Available online at www.sciencedirect.com
ScienceDirect
Comput. Methods Appl. Mech. Engrg. 417 (2023) 116413
Computer methods in applied mechanics and engineering
www.elsevier.com/locate/cma

An efficient displacement-based isogeometric formulation for geometrically exact viscoelastic beams

Giulio Ferri, Diego Ignesti, Enzo Marino*

Department of Civil and Environmental Engineering, University of Florence, Via di S. Marta 3, 50139 Firenze, Italy

Received 7 July 2023; received in revised form 25 August 2023; accepted 26 August 2023
Available online xxxx

Abstract

We propose a novel approach to the linear viscoelastic problem of shear-deformable geometrically exact beams. The generalized Maxwell model for one-dimensional solids is here efficiently extended to the case of arbitrarily curved beams undergoing finite displacement and rotations. High efficiency is achieved by combining a series of distinguishing features, that are: (i) the formulation is displacement-based, therefore no additional unknowns, other than incremental displacements and rotations, are needed for the internal variables associated with the rate-dependent material; (ii) the governing equations are discretized in space using the isogeometric collocation method, meaning that elements integration is totally bypassed; (iii) finite rotations are updated using the incremental rotation vector, leading to two main benefits: minimum number of rotation unknowns (the three components of the incremental rotation vector) and no singularity problems; (iv) the same SO(3)-consistent linearization of the governing equations and update procedures as for non-rate-dependent linear elastic material can be used; (v) a standard second-order accurate time integration scheme is made consistent with the underlying geometric structure of the kinematic problem. Moreover, taking full advantage of the isogeometric analysis features, the formulation permits accurately representing beams and beam structures with highly complex initial shape and topology, paving the way for a large number of potential applications in the field of architectured materials, meta-materials, morphing/programmable objects, topological optimizations, etc. Numerical applications are finally presented in order to demonstrate attributes and potentialities of the proposed formulation.

Keywords: Viscoelastic beams; Generalized Maxwell model; Isogeometric analysis; Geometrically nonlinear beams; Curved beams; Finite rotations

1. Introduction

The interest in designing materials with predetermined mechanical properties or objects that can change shape and function over time in a programmed way is dramatically growing due to the enormous potential that can be unlocked by emerging additive manufacturing techniques. Hybrid and architectured materials [1,2] are examples of new "materials" obtainable by assembling two or more materials, possibly with a specific voids-matter distribution,

* Corresponding author.
E-mail address: enzo.marino@unifi.it (E. Marino).

https://doi.org/10.1016/j.cma.2023.116413

such that they can exhibit attributes not owned by any (continuous distribution) of the individual materials. This principle is valid and applicable at micro [3–5], meso [6–8], and macro [9–14] length scales. In many cases, the inner architectures are assemblies of elements that individually can be well represented by one-dimensional deformable solids [15,16]. Programming this type of structures represents a complex inverse problem since the design space, in addition to the properties of the single materials, comprises topology (e.g. cell shape and fibers orientation), number and connectivity of the one-dimensional elements, their (possibly locally varying) initial curvature, composition of possible multi-layered cross sections, and other parameters [4,17,18].

For such complex systems, since three-dimensional continuum-based theories would lead to prohibitive computational costs, advanced beam theories, deployed through appropriate computational formulations, can have a tremendous impact on the predictive capabilities of the numerical models. There are some essential requirements that these theories must meet: the underlying kinematic model must be able to reproduce finite displacements and rotations without any restrictions; any three-dimensional initial geometry, possibly featured by strong and local variations of curvatures, must be accurately represented; proper nonlinear material models, including rate and temperature dependent ones, need to be supported and adapted to the one-dimensional case.

From the kinematics standpoint, starting from the fundamental works by Simo [19,20] and Cardona & Geradin [21], a number of valuable contributions have been given to the development of large deformation space beams, both to shear-deformable [22–32] and Euler–Bernoulli formulations [33–37]. These works are all restricted to linear elastic materials. Inelastic material models were initially proposed in [38–40]. More recently, elastoplasticity has been addressed in [41–43]. General three-dimensional constitutive laws are adapted to geometrically exact beams in [44–49], and in [50,51] considering also deformable directors. Focusing on viscoelasticity, finite difference schemes are used in [52–54] with a quaternion-based parametrization of finite rotations and in [55] using the special Euclidean group for the beam kinematics. Finite element formulations with applications to multi-body dynamics are proposed in [56–58].

Only recently, geometrical and material nonlinearities have been combined to specifically address the problem of programmable structures. In [59] a fully isogeometric model for geometrically exact space beams with spatially varying geometric and material properties is proposed. The possibility of modeling composite rods [60] (e.g., with bilayers [13,61]) enables bending and twisting deformations to morph one-dimensional rods into three-dimensional shapes. In [62], although a linear elastic material is used, the advantages of a geometrically exact formulation are exploited to optimize curved beams in the sense of matching target shapes for the beam axis. In [63–65], a discrete geometrically exact formulation encompassing constitutive models for incompressible viscous fluids and viscoelastic one-dimensional solids is proposed and used for simulating active and shape-morphing structures. Linear viscoelastic materials in a co-rotational setting are modeled in [66], an elasto-visco-plastic material model is proposed in [67], while a two-scale approach for nonlinear hyperelastic beams is introduced in [68]. Functionally graded beams, which are also relevant for material programming, are discussed in [59,69].

Given the key role of time- and strain rate-dependency for active materials [66,70–73] and considered the strong need for more efficient beam formulations meeting the requirements recalled above, in this paper we propose a displacement-based isogeometric collocation (IGA-C) scheme for linear viscoelastic geometrically exact beams. IGA-C [74–76] keeps the attributes of classical isogeometric analysis [77,78] and, being based on the discretization of the strong form of the governing equations, completely bypasses the issues related to elements integration. The method ensures high efficiency since it requires only one evaluation point per degree of freedom, regardless of the approximation degree [79]. IGA-C proved excellent performances for a wide range of problems [74,75,79–82,82–97], including the geometrically exact beam problem [98–102].

It is also important to mention that the relevance of geometrically nonlinear viscoelastic beams is not limited to metamaterials and architectured devices. Several applications can be found in the civil and industrial engineering sectors too (e.g., cable structures, synthetic mooring lines in offshore engineering, flexible mechanical components, etc.).

In the present work, the generalized Maxwell model for one-dimensional solids is efficiently extended to the case of arbitrarily curved beams undergoing finite displacement and rotations. High efficiency is sought by combining a series of desirable and distinguishing features, in addition to the intrinsic properties of the collocation method itself. They are: (i) The formulation is displacement-based: we demonstrate that no additional unknowns with respect to the linear elastic case are needed due to the internal variables associated with the rate-dependent material. Namely, incremental displacements and rotations are the only needed unknowns; (ii) Finite rotations are updated using the

incremental rotation vector, leading to two main benefits: minimum number of rotation unknowns (i.e., the three components of the incremental rotation vector only) and no singularity problems as opposed to the case of total rotation vector; (iii) The same SO(3)-consistent linearization of the governing equations and update procedures as for linear elastic materials (see [98,100–102]) can be directly used, meaning that no additional complexity in the construction the tangent matrix is introduced by the viscoelastic material; (iv) A standard second-order accurate time integrator is made consistent with the underlying geometric structure of the kinematic problem.

In this work we also extend to the nonlinear and rate-depended case the capabilities recently developed in [103] in order to address beams and beam structures with highly complex initial curvature.

The outline of the paper is as follows. In Section 2 we review the governing equations for the quasi-static problem and the rate-dependent material model. In Section 3 we introduce the three main steps to derive the formulation: time discretization, SO(3)-consistent linearization, and space discretization. In Section 4 we show through several numerical applications with increasing complexity the capabilities of the proposed formulation. Finally, in Section 5, we summarize and draw the main conclusions of our work.

2. Governing equations

In this section, we first introduce the strong form of the governing equations and then formulate the linear viscoelastic beam problem in a displacement-based form.

2.1. Strong form of the balance equations

Let $s \mapsto \boldsymbol{c}(s) \in \mathbb{R}^3$ be a space curve representing the axis of a beam, where $s \in [0, L] \subset \mathbb{R}$ is the arc length parameterization.

The governing equations in the strong form are given in the spatial setting as follows [19]

$$\boldsymbol{n}_{,s} + \bar{\boldsymbol{n}} = \boldsymbol{0}\,, \tag{1}$$

$$\boldsymbol{m}_{,s} + \boldsymbol{c}_{,s} \times \boldsymbol{n} + \bar{\boldsymbol{m}} = \boldsymbol{0}\,, \tag{2}$$

valid for any $s \in (0, L)$ and time instant $t \in [0, T] \subset \mathbb{R}$. L and T are the upper bounds of the space and time domains, respectively. In the above equations, $\boldsymbol{n}$ and $\boldsymbol{m}$ denote the internal forces and couples per-unit length, respectively, whereas $\bar{\boldsymbol{n}}$ and $\bar{\boldsymbol{m}}$ are the external distributed forces and couples. Boundary conditions in the spatial setting write as follows

$$\boldsymbol{\eta} = \bar{\boldsymbol{\eta}}_c \quad \text{or} \quad \boldsymbol{n} = \bar{\boldsymbol{n}}_c \quad \text{with} \quad s = \{0, L\}\,, t \in [0, T]\,, \tag{3}$$

$$\boldsymbol{\vartheta} = \bar{\boldsymbol{\vartheta}}_c \quad \text{or} \quad \boldsymbol{m} = \bar{\boldsymbol{m}}_c \quad \text{with} \quad s = \{0, L\}\,, t \in [0, T]\,, \tag{4}$$

where $\bar{\boldsymbol{\eta}}_c$ and $\bar{\boldsymbol{\vartheta}}_c$ are the spatial displacements and rotations imposed to any of the beam ends, $\bar{\boldsymbol{n}}_c$ and $\bar{\boldsymbol{m}}_c$ are the external concentrated forces and moments applied to any of the beam ends.

Eqs. (1) and (2) can be pulled-back in the material form as follows

$$\widetilde{\boldsymbol{K}}\boldsymbol{N} + \boldsymbol{N}_{,s} + \mathbf{R}^{\mathsf{T}}\bar{\boldsymbol{n}} = \boldsymbol{0}\,, \tag{5}$$

$$\widetilde{\boldsymbol{K}}\boldsymbol{M} + \boldsymbol{M}_{,s} + \left(\mathbf{R}^{\mathsf{T}}\boldsymbol{c}_{,s}\right) \times \boldsymbol{N} + \mathbf{R}^{\mathsf{T}}\bar{\boldsymbol{m}} = \boldsymbol{0}\,, \tag{6}$$

where $s \mapsto \mathbf{R}(s) \in \mathrm{SO}(3)$ is the rotation operator mapping the (rigid) rotation of the beam cross section at s from the material to the current configuration. Note that to obtain the above material form of the balance equations, we exploited the orthogonality of $\mathbf{R}$ and the (material) beam curvature, a skew-symmetric tensor defined as $s \mapsto \widetilde{\boldsymbol{K}}(s) := \mathbf{R}^{\mathsf{T}}\mathbf{R}_{,s} \in \mathrm{so}(3)$.[1] Moreover, $\boldsymbol{N} = \mathbf{R}^{\mathsf{T}}\boldsymbol{n}$ and $\boldsymbol{M} = \mathbf{R}^{\mathsf{T}}\boldsymbol{m}$ are the internal forces and couples per-unit length in the material form, respectively. Similar transformations apply to the boundary conditions.

[1] With the symbol $\sim$ we mark elements of so(3), that is the set of 3×3 skew-symmetric matrices. In this context, they are used to represent curvature matrices and infinitesimal incremental rotations. Furthermore, we recall that for any skew-symmetric matrix $\widetilde{\boldsymbol{a}} \in \mathrm{so}(3)$, $\boldsymbol{a} = \mathrm{axial}(\widetilde{\boldsymbol{a}})$ indicates the axial vector of $\widetilde{\boldsymbol{a}}$ such that $\widetilde{\boldsymbol{a}}\boldsymbol{h} = \boldsymbol{a} \times \boldsymbol{h}$, for any $\boldsymbol{h} \in \mathbb{R}^3$, where $\times$ is the cross product.

2.2. The generalized Maxwell model for one-dimensional problems

To reproduce the viscoelastic material behavior, here we employ the generalized Maxwell model [104] directly to the one-dimensional strain measures. We first recall the material form of the strain measures [19,105,106]

$$\boldsymbol{\Gamma}_N = \boldsymbol{\Gamma} - \boldsymbol{\Gamma}_0 = \mathbf{R}^\mathsf{T}\boldsymbol{c}_{,s} - \mathbf{R}_0{}^\mathsf{T}\boldsymbol{c}_{0,s} \quad \text{and} \quad \boldsymbol{K}_M = \text{axial}(\widetilde{\boldsymbol{K}} - \widetilde{\boldsymbol{K}}_0) = \boldsymbol{K} - \boldsymbol{K}_0\,, \tag{7}$$

where $\boldsymbol{\Gamma} = \mathbf{R}^\mathsf{T}\boldsymbol{c}_{,s} - [1,\,0,\,0]^\mathsf{T}$ and $\boldsymbol{\Gamma}_0 = \mathbf{R}_0{}^\mathsf{T}\boldsymbol{c}_{0,s} - [1,\,0,\,0]^\mathsf{T}$. $\boldsymbol{\Gamma}_N \in \mathbb{R}^3$ describes the axial and shear strains, whereas $\boldsymbol{K}_M \in \mathbb{R}^3$ describes the bending and torsional strains; $\widetilde{\boldsymbol{K}}_0 = \mathbf{R}_0{}^\mathsf{T}\mathbf{R}_{0,s} \in \text{so}(3)$ is the beam initial curvature (skew-symmetric tensor) in the material form; $\boldsymbol{c}_0$ represents the beam axis in the initial configuration; $\mathbf{R}_0 \in \text{SO}(3)$ is the rotation operator that expresses the rotation of the beam cross section in the initial configuration.

Assuming a rheological model made of m spring-dashpot elements, the material form of the total internal forces and couples can be written as

$$\boldsymbol{N} = \boldsymbol{N}_\infty + \sum_{\alpha=1}^{m} \boldsymbol{N}_\alpha \quad \text{and} \quad \boldsymbol{M} = \boldsymbol{M}_\infty + \sum_{\alpha=1}^{m} \boldsymbol{M}_\alpha\,, \tag{8}$$

where $\boldsymbol{N}_\infty$ and $\boldsymbol{M}_\infty$ are the long-term elastic internal forces and couples, whereas $\boldsymbol{N}_\alpha$ and $\boldsymbol{M}_\alpha$ are the viscous contributions related to the αth Maxwell element. Assuming the existence of a one-dimensional dissipative potential, additively made of a contribution related to axial and shear strains and a contribution related to torsional and bending strains (see also [53,67]), the dissipative internal stresses are given by

$$\boldsymbol{N}_\alpha = \mathbb{H}^v_{N\alpha}\dot{\boldsymbol{\Gamma}}_{N\alpha} \quad \text{and} \quad \boldsymbol{M}_\alpha = \mathbb{H}^v_{M\alpha}\dot{\boldsymbol{K}}_{M\alpha}\,, \tag{9}$$

where $\dot{\boldsymbol{\Gamma}}_{N\alpha}$ and $\dot{\boldsymbol{K}}_{M\alpha}$ are the viscous strain rate vectors and $\mathbb{H}^v_{N\alpha}$ and $\mathbb{H}^v_{M\alpha}$ are diagonal viscosity matrices associated with the αth Maxwell element. Introducing the relaxation times, τ_α with $\alpha = 1, \dots, m$, that without loss of generality are assumed to be the same for all the strain measures, the rates of viscous strains for the αth Maxwell element can be expressed through the evolutionary equations as follows

$$\dot{\boldsymbol{\Gamma}}_{N\alpha} = \frac{1}{\tau_\alpha}\left(\boldsymbol{\Gamma}_N - \boldsymbol{\Gamma}_{N\alpha}\right) \quad \text{and} \quad \dot{\boldsymbol{K}}_{M\alpha} = \frac{1}{\tau_\alpha}\left(\boldsymbol{K}_M - \boldsymbol{K}_{M\alpha}\right). \tag{10}$$

Finally, assuming that the elastic response is linear, the total material internal forces and couples become

$$\boldsymbol{N} = \mathbb{C}_{N\infty}\boldsymbol{\Gamma}_N + \sum_{\alpha=1}^{m} \mathbb{C}^v_{N\alpha}(\boldsymbol{\Gamma}_N - \boldsymbol{\Gamma}_{N\alpha})\,, \tag{11}$$

$$\boldsymbol{M} = \mathbb{C}_{M\infty}\boldsymbol{K}_M + \sum_{\alpha=1}^{m} \mathbb{C}^v_{M\alpha}(\boldsymbol{K}_M - \boldsymbol{K}_{M\alpha})\,, \tag{12}$$

with

$$\mathbb{C}_{N\infty} = \text{diag}(E_\infty A, G_\infty A_2, G_\infty A_3) \quad \text{and} \quad \mathbb{C}_{M\infty} = \text{diag}(G_\infty J_t, E_\infty J_2, E_\infty J_3)\,,$$

$$\mathbb{C}^v_{N\alpha} = \mathbb{H}^v_{N\alpha}/\tau_\alpha = \text{diag}(E_\alpha A, G_\alpha A_2, G_\alpha A_3) \quad \text{and} \quad \mathbb{C}^v_{M\alpha} = \mathbb{H}^v_{M\alpha}/\tau_\alpha = \text{diag}(G_\alpha J_t, E_\alpha J_2, E_\alpha J_3)\,,$$

where E_∞ and $G_\infty = E_\infty/2(1+\nu)$ are the long term Young and shear moduli, whereas E_α and $G_\alpha = E_\alpha/2(1+\nu)$ are the Young and shear moduli associated with the αth Maxwell element. We assume a constant Poisson ratio for the material.

2.3. Displacement-based strong form of the governing equations

By substituting Eqs. (11) and (12) into (5) and (6), we obtain the governing equations expressed in terms of kinematic quantities only, i.e. total and viscous strain measures, as follows

$$\widetilde{\boldsymbol{K}}\mathbb{C}_{N0}\boldsymbol{\Gamma}_N - \widetilde{\boldsymbol{K}}\sum_{\alpha=1}^{m} \mathbb{C}^v_{N\alpha}\boldsymbol{\Gamma}_{N\alpha} + \mathbb{C}_{N0}\boldsymbol{\Gamma}_{N,s} - \sum_{\alpha=1}^{m} \mathbb{C}^v_{N\alpha}\boldsymbol{\Gamma}_{N\alpha,s} + \mathbf{R}^\mathsf{T}\bar{\boldsymbol{n}} = \mathbf{0}\,, \tag{13}$$

$$\widetilde{\boldsymbol{K}}\mathbb{C}_{M0}\boldsymbol{K}_M - \widetilde{\boldsymbol{K}}\sum_{\alpha=1}^{m}\mathbb{C}^v_{M\alpha}\boldsymbol{K}_{M\alpha} + \mathbb{C}_{M0}\boldsymbol{K}_{M,s} - \sum_{\alpha=1}^{m}\mathbb{C}^v_{M\alpha}\boldsymbol{K}_{M\alpha,s} + \mathbf{R}^{\mathsf{T}}\boldsymbol{c}_{,s}\times\mathbb{C}_{N0}\boldsymbol{\Gamma}_N +$$
$$-\mathbf{R}^{\mathsf{T}}\boldsymbol{c}_{,s}\times\sum_{\alpha=1}^{m}\mathbb{C}^v_{N\alpha}\boldsymbol{\Gamma}_{N\alpha} + \mathbf{R}^{\mathsf{T}}\bar{\boldsymbol{m}} = \mathbf{0}\,. \tag{14}$$

Similarly, the Neumann boundary conditions become

$$\mathbb{C}_{N0}\boldsymbol{\Gamma}_N - \sum_{\alpha=1}^{m}\mathbb{C}^v_{N\alpha}\boldsymbol{\Gamma}_{N\alpha} = \mathbf{R}^{\mathsf{T}}\bar{\boldsymbol{n}}_c\,, \tag{15}$$

$$\mathbb{C}_{M0}\boldsymbol{K}_M - \sum_{\alpha=1}^{m}\mathbb{C}^v_{M\alpha}\boldsymbol{K}_{M\alpha} = \mathbf{R}^{\mathsf{T}}\bar{\boldsymbol{m}}_c\,, \tag{16}$$

where $\mathbb{C}_{N0} = \mathbb{C}_{N\infty} + \sum_{\alpha=1}^{m}\mathbb{C}^v_{N\alpha}$ and $\mathbb{C}_{M0} = \mathbb{C}_{M\infty} + \sum_{\alpha=1}^{m}\mathbb{C}^v_{M\alpha}$ are the instantaneous elasticity tensors.

3. Discretization and consistent linearization of the governing equations

In this section, after introducing the time discretization, we present the consistent linearization and space discretization of the governing equations.

3.1. Time discretization and integration scheme

By using the standard trapezoidal rule for the time integration, at time $t^n = (n-1)dt$, where dt is the time step span and $n = 1, \dots$ is the time step counter, the time discretized viscous strain measures $\boldsymbol{\Gamma}^n_{N\alpha}$ and $\boldsymbol{K}^n_{N\alpha}$ associated with the αth Maxwell element can be expressed as

$$\boldsymbol{\Gamma}^n_{N\alpha} = \frac{dt}{(2\tau_\alpha + dt)}\,\boldsymbol{\Gamma}^n_N + \boldsymbol{\beta}^{n-1}_{\Gamma\alpha}\,, \tag{17}$$

$$\boldsymbol{K}^n_{N\alpha} = \frac{dt}{(2\tau_\alpha + dt)}\,\boldsymbol{K}^n_M + \boldsymbol{\beta}^{n-1}_{K\alpha}\,, \tag{18}$$

where the terms $\boldsymbol{\beta}^{n-1}_{\Gamma\alpha}$ and $\boldsymbol{\beta}^{n-1}_{K\alpha}$ are defined as follows

$$\boldsymbol{\beta}^{n-1}_{\Gamma\alpha} = \frac{dt}{(2\tau_\alpha + dt)}\,\boldsymbol{\Gamma}^{n-1}_N + \frac{2\tau_\alpha - dt}{(2\tau_\alpha + dt)}\,\boldsymbol{\Gamma}^{n-1}_{N\alpha}\,, \tag{19}$$

$$\boldsymbol{\beta}^{n-1}_{K\alpha} = \frac{dt}{(2\tau_\alpha + dt)}\,\boldsymbol{K}^{n-1}_M + \frac{2\tau_\alpha - dt}{(2\tau_\alpha + dt)}\,\boldsymbol{K}^{n-1}_{M\alpha}\,. \tag{20}$$

Importantly, we remark that the above terms are computed using only quantities known form the previous time step, therefore they do not need to be iteratively updated during the Newton–Raphson algorithm.

Substituting Eqs. (17) and (18) into the time discretized form of Eqs. (13) and (14), the nonlinear governing equations can be expressed in terms of total strains (and other quantities known from the previous time step) as follows

$$\widetilde{\boldsymbol{K}}^n[\mathbb{C}_{N0} - \sum_{\alpha=1}^{m}\mathbb{C}^v_{N\alpha}\frac{dt}{(2\tau_\alpha + dt)}]\boldsymbol{\Gamma}^n_N - \widetilde{\boldsymbol{K}}^n\sum_{\alpha=1}^{m}\mathbb{C}^v_{N\alpha}\boldsymbol{\beta}^{n-1}_{\Gamma\alpha} +$$
$$+[\mathbb{C}_{N0} - \sum_{\alpha=1}^{m}\mathbb{C}^v_{N\alpha}\frac{dt}{(2\tau_\alpha + dt)}]\boldsymbol{\Gamma}^n_{N,s} - \sum_{\alpha=1}^{m}\mathbb{C}^v_{N\alpha}\boldsymbol{\beta}^{n-1}_{\Gamma\alpha,s} + \mathbf{R}^{\mathsf{T}^n}\bar{\boldsymbol{n}}^n = \mathbf{0}\,, \tag{21}$$

$$\widetilde{\boldsymbol{K}}^n[\mathbb{C}_{M0} - \sum_{\alpha=1}^{m}\mathbb{C}^v_{M\alpha}\frac{dt}{(2\tau_\alpha + dt)}]\boldsymbol{K}^n_M + [\mathbb{C}_{M0} - \sum_{\alpha=1}^{m}\mathbb{C}^v_{M\alpha}\frac{dt}{(2\tau_\alpha + dt)}]\boldsymbol{K}^n_{M,s} +$$
$$-\widetilde{\boldsymbol{K}}^n\sum_{\alpha=1}^{m}\mathbb{C}^v_{M\alpha}\boldsymbol{\beta}^{n-1}_{K\alpha} - \sum_{\alpha=1}^{m}\mathbb{C}^v_{M\alpha}\boldsymbol{\beta}^{n-1}_{K\alpha,s} + \mathbf{R}^{\mathsf{T}^n}\boldsymbol{c}^n{}_{,s}\times[\mathbb{C}_{N0} - \sum_{\alpha=1}^{m}\mathbb{C}^v_{N\alpha}\frac{dt}{(2\tau_\alpha + dt)}]\boldsymbol{\Gamma}^n_N +$$
$$-\mathbf{R}^{\mathsf{T}^n}\boldsymbol{c}^n{}_{,s}\times\sum_{\alpha=1}^{m}\mathbb{C}^v_{N\alpha}\boldsymbol{\beta}^{n-1}_{\Gamma\alpha} + \mathbf{R}^{\mathsf{T}^n}\bar{\boldsymbol{m}}^n = \mathbf{0}\,. \tag{22}$$

The same can be done for the Neumann boundary conditions

$$[\mathbb{C}_{N0} - \sum_{\alpha=1}^{m} \mathbb{C}^{v}_{N\alpha} \frac{dt}{(2\tau_\alpha + dt)}] \boldsymbol{\Gamma}^{n}_{N} = \sum_{\alpha=1}^{m} \mathbb{C}^{v}_{N\alpha} \boldsymbol{\beta}^{n-1}_{\Gamma\alpha} + \mathbf{R}^{\mathsf{T}n} \bar{\boldsymbol{n}}^{n}_{c} \,, \tag{23}$$

$$[\mathbb{C}_{M0} - \sum_{\alpha=1}^{m} \mathbb{C}^{v}_{M\alpha} \frac{dt}{(2\tau_\alpha + dt)}] \boldsymbol{K}^{n}_{M} = \sum_{\alpha=1}^{m} \mathbb{C}^{v}_{M\alpha} \boldsymbol{\beta}^{n-1}_{K\alpha} + \mathbf{R}^{\mathsf{T}n} \bar{\boldsymbol{m}}^{n}_{c} \,. \tag{24}$$

3.2. SO(3)-*consistent linearization of the displacement-based governing equations*

A remarkable feature of the present formulation is that the same SO(3)-consistent linearization rules derived for static or dynamic formulations with non rate-dependent material, see, e.g., [102], can be directly used. This is possible since, as noticed above, the viscous components can be expressed by terms depending on the total strains (likewise the non-rate-dependent case) and terms ($\boldsymbol{\beta}^{n-1}_{\Gamma\alpha}$ and $\boldsymbol{\beta}^{n-1}_{K\alpha}$) which are known from the previous time step and therefore do not substantially affect the construction of the tangent operator.

To preserve SO(3)-consistency, we only recall some fundamental geometrical aspects. Given a curve in the configuration manifold $\varepsilon \mapsto \boldsymbol{\gamma}(\varepsilon) = (\boldsymbol{c}_\varepsilon, \mathbf{R}_\varepsilon)$, with $\varepsilon \in \mathbb{R}$, defined by $\boldsymbol{c}_\varepsilon = \boldsymbol{c} + \varepsilon\delta\boldsymbol{\eta}$ (standard translation on $\mathbb{R}^3$) and $\mathbf{R}_\varepsilon = \mathbf{R}\exp(\varepsilon\delta\widetilde{\boldsymbol{\Theta}})$ (left translation on SO(3)), the linearization is based on the construction of the (material) tangent space at $(\boldsymbol{c}, \mathbf{R})$ obtained by $(d\boldsymbol{\gamma}/d\varepsilon)_{\varepsilon=0}$ such that $\boldsymbol{\gamma}(0) = (\boldsymbol{c}, \mathbf{R})$. From the kinematic point of view, $\delta\boldsymbol{\eta} \in \mathbb{R}^3$ represents an incremental displacement superimposed to the current configuration of the centroid line $\boldsymbol{c}$; whereas $\delta\widetilde{\boldsymbol{\Theta}} \in$ so(3) represents an incremental rotation superimposed to the rotation $\mathbf{R}$. Note that in the construction of the curve $\boldsymbol{\gamma}$ we used the exponential map exp : so(3) $\to$ SO(3) which maps the line $\varepsilon\widetilde{\boldsymbol{\Theta}}$ at so(3) onto the one parameter subgroup $\exp(\varepsilon\widetilde{\boldsymbol{\Theta}}) \in$ SO(3) [107]. Note that for SO(3) the exponential map is expressed by an exact (Rodrigues) formula.

By using the linearization rules given in [102], the linearized version of Eqs. (21)–(24) is

$$\begin{aligned}
&[\bar{\mathbb{C}}_N(\widetilde{\hat{\mathbf{R}}^{\mathsf{T}n}\hat{\boldsymbol{c}}^{n}_{,s}}) - (\widetilde{\bar{\mathbb{C}}_N\hat{\boldsymbol{\Gamma}}^{n}_{N}}) + \sum_{\alpha=1}^{m}(\widetilde{\mathbb{C}^{v}_{N\alpha}\boldsymbol{\beta}^{n-1}_{\Gamma\alpha}})]\delta\boldsymbol{\Theta}^{,n}_{,s} + \\
&+[\hat{\widetilde{\boldsymbol{K}}}^{n}\bar{\mathbb{C}}_N(\widetilde{\hat{\mathbf{R}}^{\mathsf{T}n}\hat{\boldsymbol{c}}^{n}_{,s}}) - (\widetilde{\bar{\mathbb{C}}_N\hat{\boldsymbol{\Gamma}}^{n}_{N}})\hat{\widetilde{\boldsymbol{K}}}^{n} + \hat{\widetilde{\boldsymbol{K}}}^{n}\sum_{\alpha=1}^{m}(\widetilde{\mathbb{C}^{v}_{N\alpha}\boldsymbol{\beta}^{n-1}_{\Gamma\alpha}}) - (\hat{\widetilde{\boldsymbol{K}}}^{n}\widetilde{\sum_{\alpha=1}^{m}\mathbb{C}^{v}_{N\alpha}\boldsymbol{\beta}^{n-1}_{\Gamma\alpha}}) + \\
&+\bar{\mathbb{C}}_N(\widetilde{\hat{\mathbf{R}}^{\mathsf{T}n}\hat{\boldsymbol{c}}^{n}_{,ss}}) - \bar{\mathbb{C}}_N(\widetilde{\tilde{\boldsymbol{K}}^{n}\hat{\mathbf{R}}^{\mathsf{T}n}\hat{\boldsymbol{c}}^{n}_{,s}}) + (\widetilde{\hat{\mathbf{R}}^{\mathsf{T}n}\bar{\boldsymbol{n}}^{n}})]\delta\boldsymbol{\Theta}^{n} + \bar{\mathbb{C}}_N\hat{\mathbf{R}}^{\mathsf{T}n}\delta\boldsymbol{\eta}^{n}_{,ss} + \\
&+[\tilde{\boldsymbol{K}}^{n}\bar{\mathbb{C}}_N\hat{\mathbf{R}}^{\mathsf{T}n} - \bar{\mathbb{C}}_N\tilde{\boldsymbol{K}}^{n}\hat{\mathbf{R}}^{\mathsf{T}n}]\delta\boldsymbol{\eta}^{n}_{,s} + \hat{\mathbf{F}}^{n} = \mathbf{0} \,,
\end{aligned} \tag{25}$$

$$\begin{aligned}
&\bar{\mathbb{C}}_M\delta\boldsymbol{\Theta}^{,n}_{,ss} + [\bar{\mathbb{C}}_M\hat{\widetilde{\boldsymbol{K}}}^{n} + \hat{\widetilde{\boldsymbol{K}}}^{n}\bar{\mathbb{C}}_M - (\widetilde{\bar{\mathbb{C}}_M\hat{\boldsymbol{K}}^{n}_{M}}) + \sum_{\alpha=1}^{m}(\widetilde{\mathbb{C}^{v}_{M\alpha}\boldsymbol{\beta}^{n-1}_{K\alpha}})]\delta\boldsymbol{\Theta}^{,n}_{,s} + \\
&+[\hat{\widetilde{\boldsymbol{K}}}^{n}\bar{\mathbb{C}}_M\hat{\widetilde{\boldsymbol{K}}}^{n} - (\widetilde{\bar{\mathbb{C}}_M\hat{\boldsymbol{K}}^{n}_{M}})\hat{\widetilde{\boldsymbol{K}}}^{n} + \hat{\widetilde{\boldsymbol{K}}}^{n}\sum_{\alpha=1}^{m}(\widetilde{\mathbb{C}^{v}_{M\alpha}\boldsymbol{\beta}^{n-1}_{K\alpha}}) - (\hat{\widetilde{\boldsymbol{K}}}^{n}\widetilde{\sum_{\alpha=1}^{m}\mathbb{C}^{v}_{M\alpha}\boldsymbol{\beta}^{n-1}_{K\alpha}}) + \\
&+\bar{\mathbb{C}}_M\hat{\widetilde{\boldsymbol{K}}}^{n}_{,s} + [(\widetilde{\hat{\mathbf{R}}^{\mathsf{T}n}\hat{\boldsymbol{c}}^{n}_{,s}})\bar{\mathbb{C}}_N - (\widetilde{\bar{\mathbb{C}}_N\hat{\boldsymbol{\Gamma}}^{n}_{N}}) + \sum_{\alpha=1}^{m}(\widetilde{\mathbb{C}^{v}_{N\alpha}\boldsymbol{\beta}^{n-1}_{\Gamma\alpha}})](\widetilde{\hat{\mathbf{R}}^{\mathsf{T}n}\hat{\boldsymbol{c}}^{n}_{,s}}) + (\widetilde{\hat{\mathbf{R}}^{\mathsf{T}n}\bar{\boldsymbol{m}}^{n}})]\delta\boldsymbol{\Theta}^{n} + \\
&+[(\widetilde{\hat{\mathbf{R}}^{\mathsf{T}n}\hat{\boldsymbol{c}}^{,n}_{,s}})\bar{\mathbb{C}}_N - (\widetilde{\bar{\mathbb{C}}_N\hat{\boldsymbol{\Gamma}}^{n}_{N}}) + \sum_{\alpha=1}^{m}(\widetilde{\mathbb{C}^{v}_{N\alpha}\boldsymbol{\beta}^{n-1}_{\Gamma\alpha}})]\hat{\mathbf{R}}^{\mathsf{T}n}\delta\boldsymbol{\eta}^{n}_{,s} + \hat{\mathbf{T}}^{n} = \mathbf{0} \,,
\end{aligned} \tag{26}$$

where we have defined

$$\hat{\mathbf{F}}^{n} = \hat{\widetilde{\boldsymbol{K}}}^{n}\bar{\mathbb{C}}_N\hat{\boldsymbol{\Gamma}}^{n}_{N} - \hat{\widetilde{\boldsymbol{K}}}^{n}\sum_{\alpha=1}^{m}\mathbb{C}^{v}_{N\alpha}\boldsymbol{\beta}^{n-1}_{\Gamma\alpha} + \bar{\mathbb{C}}_N\hat{\boldsymbol{\Gamma}}^{n}_{N,s} - \sum_{\alpha=1}^{m}\mathbb{C}^{v}_{N\alpha}\boldsymbol{\beta}^{n-1}_{\Gamma\alpha,s} + \hat{\mathbf{R}}^{\mathsf{T}n}\bar{\boldsymbol{n}}^{n} \,, \tag{27}$$

$$\hat{\mathbf{T}}^n = \hat{\widetilde{\boldsymbol{K}}}^n \bar{\mathbb{C}}_M \hat{\boldsymbol{K}}^n_M - \hat{\widetilde{\boldsymbol{K}}}^n \sum_{\alpha=1}^{m} \mathbb{C}^v_{M\alpha} \boldsymbol{\beta}^{n-1}_{K\alpha} + \bar{\mathbb{C}}_M \hat{\boldsymbol{K}}^n_{M,s} - \sum_{\alpha=1}^{m} \mathbb{C}^v_{M\alpha} \boldsymbol{\beta}^{n-1}_{K\alpha,s} +$$

$$+ \hat{\mathbf{R}}^{\mathsf{T}n} \hat{\boldsymbol{c}}^n{}_{,s} \times [\bar{\mathbb{C}}_N \hat{\boldsymbol{\Gamma}}^n_N - \sum_{\alpha=1}^{m} \mathbb{C}^v_{N\alpha} \boldsymbol{\beta}^{n-1}_{\Gamma\alpha}] + \hat{\mathbf{R}}^{\mathsf{T}n} \bar{\boldsymbol{m}}^n \,, \tag{28}$$

and we have set $\bar{\mathbb{C}}_N = [\mathbb{C}_{N0} - \sum_{\alpha=1}^{m} \mathbb{C}^v_{N\alpha} \frac{dt}{(2\tau_\alpha + dt)}]$ and $\bar{\mathbb{C}}_M = [\mathbb{C}_{M0} - \sum_{\alpha=1}^{m} \mathbb{C}^v_{M\alpha} \frac{dt}{(2\tau_\alpha + dt)}]$.

Similarly, for the boundary conditions we have

$$[\bar{\mathbb{C}}_N \widetilde{(\hat{\mathbf{R}}^{\mathsf{T}n} \hat{\boldsymbol{c}}^n{}_{,s})} - \widetilde{(\hat{\mathbf{R}}^{\mathsf{T}n} \bar{\boldsymbol{n}}^n_c)}] \delta \boldsymbol{\Theta}^n + \bar{\mathbb{C}}_N \hat{\mathbf{R}}^{\mathsf{T}n} \delta \boldsymbol{\eta}^n_{,s} = \sum_{\alpha=1}^{m} \mathbb{C}^v_{N\alpha} \boldsymbol{\beta}^{n-1}_{\Gamma\alpha} - \bar{\mathbb{C}}_N \hat{\boldsymbol{\Gamma}}^n_N + \hat{\mathbf{R}}^{\mathsf{T}n} \bar{\boldsymbol{n}}^n_c \,, \tag{29}$$

and

$$\bar{\mathbb{C}}_M \delta \boldsymbol{\Theta}^n_{,s} + [\bar{\mathbb{C}}_M \hat{\widetilde{\boldsymbol{K}}}^n - \widetilde{(\hat{\mathbf{R}}^{\mathsf{T}n} \bar{\boldsymbol{m}}^n_c)}] \delta \boldsymbol{\Theta}^n = \sum_{\alpha=1}^{m} \mathbb{C}^v_{M\alpha} \boldsymbol{\beta}^{n-1}_{K\alpha} - \bar{\mathbb{C}}_M \hat{\boldsymbol{K}}^n_M + \hat{\mathbf{R}}^{\mathsf{T}n} \bar{\boldsymbol{m}}^n_c \,. \tag{30}$$

In the above linearized equations, with the symbol $\hat{(\cdot)}$ we denote any quantity evaluated at the time t^n around which the linearization takes place. Note that the linearized equations has just more terms, but do not add any significant complexity to the standard linear elastic rate-independent IGA-C formulations [98,100–102].

3.3. Space discretization

The linearized governing equations, written in terms of the unknown fields $\delta \boldsymbol{\Theta}^n$ and $\delta \boldsymbol{\eta}^n$ at time t^n, are spatially discretized by using NURBS basis functions $R_{j,p}$ with $j = 1, \ldots, \mathrm{n}$ of degree p. In the isoparametric formulation, we use the same basis functions to represent the beam centroid curve. Thus, we have

$$\delta \boldsymbol{\Theta}^n(u) = \sum_{j=1}^{\mathrm{n}} R_{j,p}(u) \delta \check{\boldsymbol{\Theta}}^n_j \quad \text{with} \quad u \in [0,\ 1] \,, \tag{31}$$

$$\delta \boldsymbol{\eta}^n(u) = \sum_{j=1}^{\mathrm{n}} R_{j,p}(u) \delta \check{\boldsymbol{\eta}}^n_j \quad \text{with} \quad u \in [0,\ 1] \,, \tag{32}$$

$$\boldsymbol{c}^n(u) = \sum_{j=1}^{\mathrm{n}} R_{j,p}(u) \check{\boldsymbol{p}}^n_j \quad \text{with} \quad u \in [0,\ 1] \,, \tag{33}$$

where $\delta \check{\boldsymbol{\Theta}}^n_j$ and $\delta \check{\boldsymbol{\eta}}^n_j$ are the primal $(2 \times 3 \times \mathrm{n})$ unknowns, namely the jth incremental control rotation and translation, respectively; $\check{\boldsymbol{p}}^n_j$ is the jth control point defining the beam centroid curve. Eqs. (31) and (32) are substituted into (25) and (26) and in the boundary conditions (29) and (30), where the differentiations must be properly done considering the Jacobian relating the parametric u and arc length s coordinate systems. A square system is finally built by collocating the field equations at the internal $\mathrm{n}-2$ collocation points and the Dirichlet or Neumann boundary conditions at the boundaries $u = 0$ and $u = 1$. Standard Greville abscissae [74] are chosen as collocation points. At a given Newton–Raphson iteration, once solved the linear system for the primal variables, we follow the same updating procedure discussed in [102] and make use Eqs. (17)–(20) to update the viscous terms which are only evaluated at the collocation points.

4. Numerical results

In this section we report a series of numerical applications aimed at testing all the attributes of the proposed model. We start with the roll-up of a straight cantilever beam under a concentrated couple at the free-end. For the same beam, we also present the results under a concentrated tip force with a complex variation in time. Then, a circular arch with an out-of plane tip load is considered. In this case, in order to check the rates of convergence in space, we keep the problem linear to use the exact solution as a reference. For all the above mentioned tests, the material properties are intentionally set to emphasize the viscoelastic behavior and to check the robustness of the proposed method. Subsequently, the capability to model curved beam problems in the nonlinear regime is tested

Table 1
Material mechanical properties for the roll-up case.

	E_α [N/m^2]	$\tau_\alpha(t \approx 0\,\text{s})$ [s]	$\tau_\alpha(t \approx t_\infty)$ [s]
$\alpha = \infty$	40	–	–
$\alpha = 1$	530	5000	0.05

starting from a circular arch and then addressing the Spivak [103] and the Lissajous [96] beams, both featuring very challenging curvatures. Finally, the full potentialities of the proposed formulation are shown by simulating the complex deformations of planar and cylindrical nets with cells made of curved beam elements.

4.1. Roll-up of a cantilever beam

The beam is placed along the x_1-axis of a fixed Cartesian reference system and is subjected to a concentrated couple at the free end with axis x_2. The length of the beam is 1 m. The cross section is a square of side 0.1 m. One Maxwell element is employed, i.e., $m = 1$. The Young modulus E_1 and relaxation time τ_1 are reported in Table 1. The shear modulus is set as $G_1 = E_1/2(1+\nu)$, where, for this specific test, $\nu = 0$. The relaxation time is $\tau_1 = 5000\,\text{s}$ to study the convergence of the instantaneous response ($t \approx 0\,\text{s}$), whereas $\tau_1 = 0.05\,\text{s}$ to study the convergence of the long term ($t \approx t_\infty$) response. In the former case the time step is $1 \times 10^{-4}\,\text{s}$, in the latter 5 s.

We apply a couple of magnitudes $M_0 = 2\pi(E_\infty + E_1)J_2/L$ and $M_\infty = 2\pi E_\infty J_2/L$, such that the beam deforms into a full closed circle of radius $L/2\pi$ at both times $t \approx 0\,\text{s}$ and $t \approx t_\infty$. We assess the quality of the convergence rates by comparing the computed position of the beam tip, $err_{tip} = \|\boldsymbol{p}_\text{n}^h\|_{L_2}$, with the exact value, namely the clamped end located at the origin of the reference system. Moreover, to have also a global measure of the error, in addition to err_{tip}, we compare also the radius of the closed circle computed numerically, r^h, with the analytical one. r^h is obtained selecting three points uniformly spaced on the deformed beam axis. The relative error is then computed as $err_{radius} = 2\pi|r^h - L/2\pi|/L$. These two errors are plotted vs. the number of collocation points and for different degrees for both instantaneous (Fig. 1) and long term (Fig. 2) responses.

It is observed that the two error measures exhibit very good spatial convergence rates for all the degrees considered both at instantaneous and infinity times. It is noted that the accuracy cannot be smaller than 1×10^{-10} due to the tolerance set in the Newton–Raphson algorithm. Odd degrees are not considered in this study since, as it is well known, in collocation they do not normally improve the rates compared to the smaller even degree.

4.2. Cantilever beam subjected to a tip force

The same cantilever beam analyzed in the previous section is here loaded with a tip force in the x_3 direction with the complex pattern shown in Fig. 3(a). The relaxation time is 0.1 s. A time step of $1 \times 10^{-3}\,\text{s}$ is used for a total simulation time of 4 s. The time history of the displacements in the x_1 and x_2 directions are shown in Figs. 3(b) and 3(c), respectively, where a comparison with Abaqus [108] is included. Our IGA-C solution is obtained with $\text{n} = 20$ collocation points and basis functions with degree $p = 6$. The same Maxwell material model adopted here (see Table 1) is assigned to Abaqus by entering the normalized values of the shear and bulk moduli for each Maxwell element and for the long term response. In order to verify our results, an Abaqus overkill solution with B31 shear-deformable beam elements has been used. As it can be noticed from Fig. 3(c), the beam undergoes large deflections. The viscous deformations are rather significant since, under repeated force steps, the deflection keeps increasing. For example, under a constant force of $4 \times 10^{-4}\,\text{N}$, from 2.25 s to 3.25 s, the vertical tip displacement increases from 0.1255 m to 0.2525 m. An excellent agreement with Abaqus is observed.

4.3. Circular arch subjected to an out-of plane tip force

The 90° circular arch here considered has a radius $R = 1\,\text{m}$ and a square cross section of side 0.1 m. The beam lies in the (x_1, x_2) plane, it is clamped at one end and subjected to a constant force along the x_3-direction applied at its free end. The beam centroid is exactly reconstructed using 3 control points and NURBS basis functions of degree 2. k-refinement is then applied. The same material properties for the long term response of the above roll-up

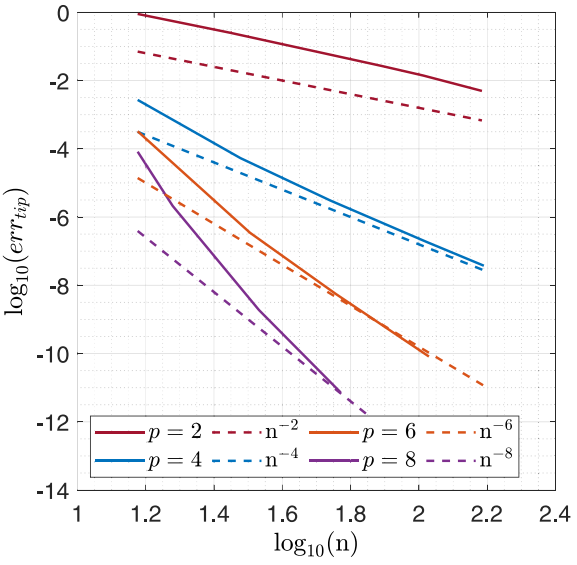

(a) Convergence plots for $p = 2, 4, 6, 8$ of err_{tip} vs. number of collocation points.

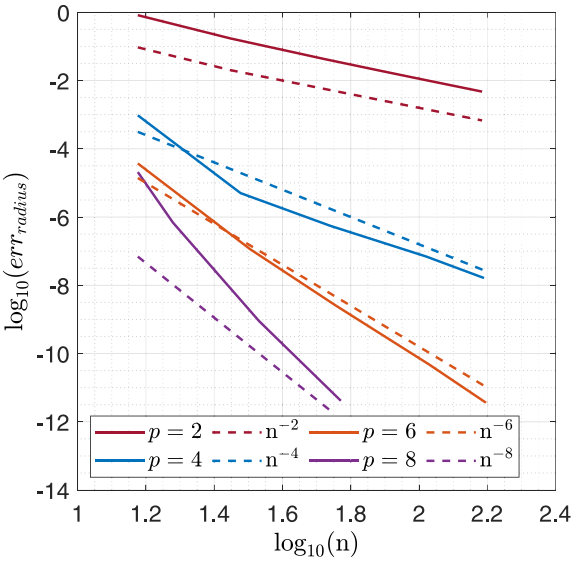

(b) Convergence plots for $p = 2, 4, 6, 8$ of err_{radius} vs. number of collocation points.

Fig. 1. Instantaneous roll-up of a viscoelastic cantilever beam: errors convergence.

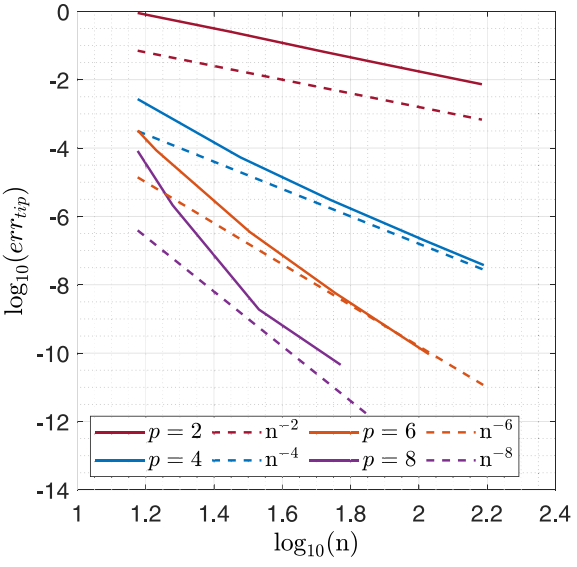

(a) Convergence plots for $p = 2, 4, 6, 8$ of err_{tip} vs. number of collocation points.

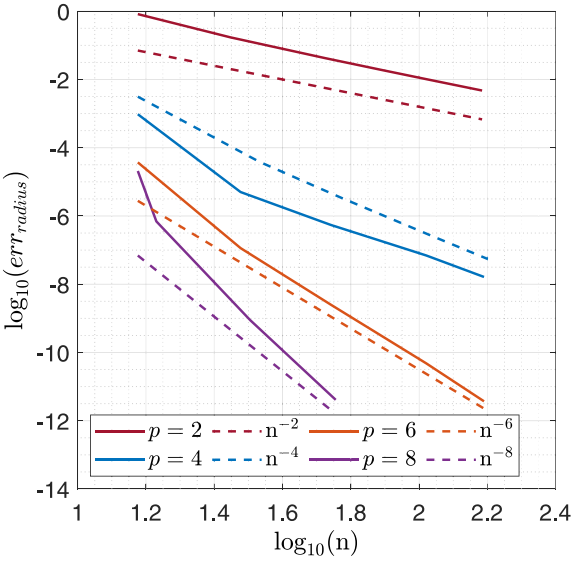

(b) Convergence plots for $p = 2, 4, 6, 8$ of err_{radius} vs. number of collocation points.

Fig. 2. Long term roll-up of a viscoelastic cantilever beam: errors convergence.

case are here employed; the time step is 0.1 s. Under the hypothesis of small displacements, the instantaneous and long term analytical solutions [85], given in terms of tip deflections v_0 and v_∞, respectively, are given by

$$v_0 = \frac{\pi F_3 R}{2 G_0 A_3} + \frac{F_3 R^3}{G_0 J_t}\left(\frac{3}{4}\pi - 2\right) + \frac{\pi F_3 R^3}{4 E_0 J_2}\,, \tag{34}$$

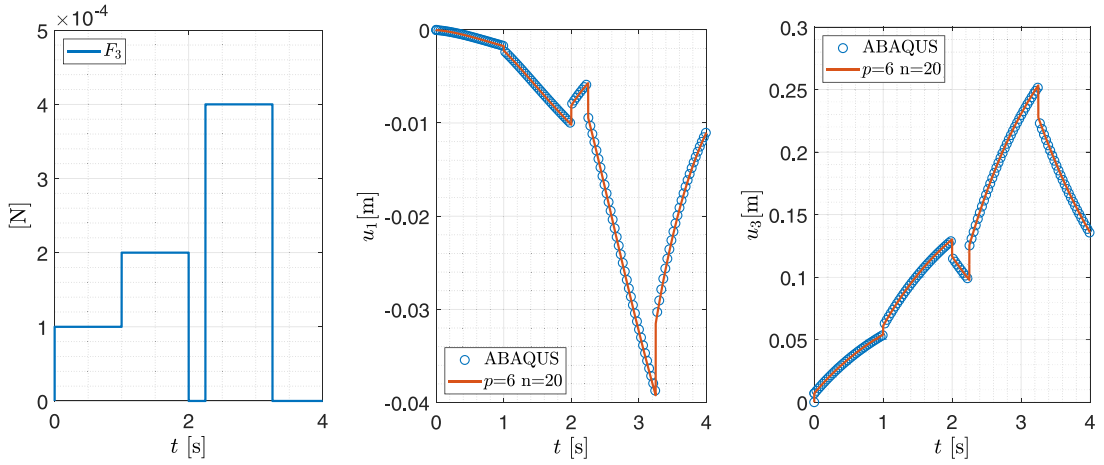

(a) Load intensity in x_3 direction.

(b) Tip displacement along the x_1-axis.

(c) Tip displacement along the x_3-axis.

Fig. 3. Cantilever beam subjected to tip load: loads and tip displacements over time.

$$v_\infty = \frac{\pi F_3 R}{2G_\infty A_3} + \frac{F_3 R^3}{G_\infty J_t}\left(\frac{3}{4}\pi - 2\right) + \frac{\pi F_3 R^3}{4E_\infty J_2}, \tag{35}$$

where $G_0 = G_\infty + G_1$, $E_0 = E_\infty + E_1$, A_3 is the beam cross section multiplied by the shear correction factor (equal to 5/6), whereas J_t and J_2 are the torsional and the bending moment of inertia, respectively. The out-of-plane force is $F_3 = 1 \times 10^{-8}$ N.

The relative errors at the beam tip for the instantaneous and the long term responses are shown in Figs. 4(a) and 4(b), respectively. Very good convergence rates are observed, although in the long term case apparently the error reaches about 1×10^{-9}, whereas for the instantaneous case it reaches 1×10^{-10} that is the tolerance limit in the Newton–Raphson algorithm.

4.4. Circular arch under complex tip load patterns

The same circular arch of the previous section is here subjected to a complex tip load pattern. As shown in Fig. 5, the tip forces and couples are applied along the x_2 and x_3 axes with time-varying intensities shown in Fig. 6. The load time histories are chosen to emphasize the viscoelastic behavior of the beam.

The total simulation time is 4 s with a time step $dt = 1 \times 10^{-3}$ s. For the space discretization we used basis functions with $p = 6$ and n = 50. A material very similar to the one used in [109], characterized by 9 Maxwell elements and $\nu = 0.4$, is employed (see Table 2).

The tip displacements in the three Cartesian directions are shown in Fig. 7. A comparison with an overkill solution obtained with Abaus (B31 elements) is also included and a very good agreement is observed. Note that the sharp variation of the displacements u_1 and u_2 at $t = 2$ s (see Figs. 7(a) and 7(b)) is associated with the complete unloading of the beam for that time instant. Such a variation is not noticeable in the x_3 direction (see Fig. 7(c)) since from $t = 1.999$ s to $t = 2.001$ s u_3 changes sign.

4.5. Spivak beam under tip loads

Moving to more complex geometrically nonlinear cases, we analyze here the Spivak beam [103]. It is a rather challenging three-dimensional geometry which permits also assessing the capability of the proposed model to reconstruct complex initial geometries featuring points with vanishing curvature. The initial beam axis is given

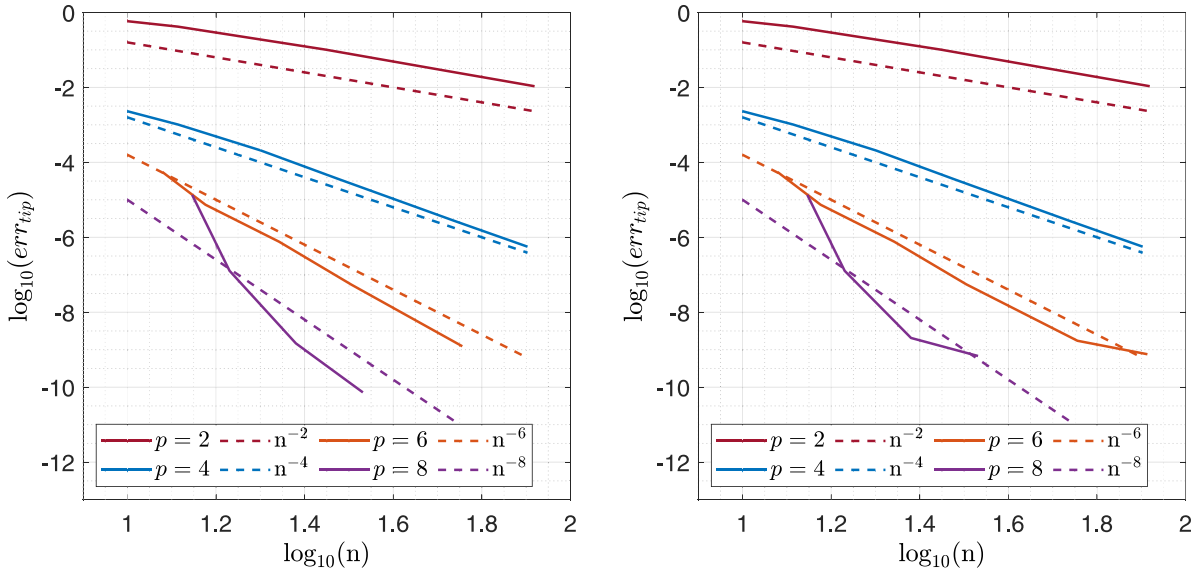

(a) Convergence plots for $p = 2, 4, 6, 8$ of err_{tip} for $t \approx 0\,\mathrm{s}$ vs. number of collocation points.

(b) Convergence plots for $p = 2, 4, 6, 8$ of err_{tip} for $t \approx t_\infty$ vs. number of collocation points.

Fig. 4. 90° circular arch subjected to an out-of plane tip force: errors convergence.

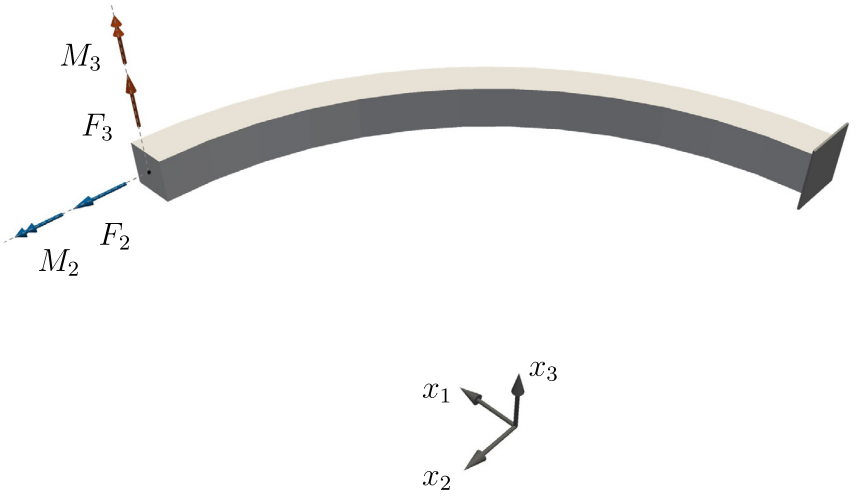

Fig. 5. 90° circular arch clamped at on end and subjected to tip forces and couples along x_2-axis (blue) and x_3-axis (orange).

by the following piecewise-defined curve

$$\begin{cases} \boldsymbol{c}(s) = [s,\ 0,\ e^{-1/s^2}]^\mathsf{T}\,, & s \in [-2, 0)\,, \\ \boldsymbol{c}(s) = [0,\ 0,\ 0]^\mathsf{T}\,, & s = 0\,, \\ \boldsymbol{c}(s) = [s,\ e^{-1/s^2},\ 0]^\mathsf{T}\,, & s \in (0, 3]. \end{cases} \tag{36}$$

The beam has a total length of 5.50 m, with a square cross section of side 0.2 m (see Fig. 8). The material is the same used in the previous case whose parameters are reported in Table 2. The beam is loaded with two tip forces

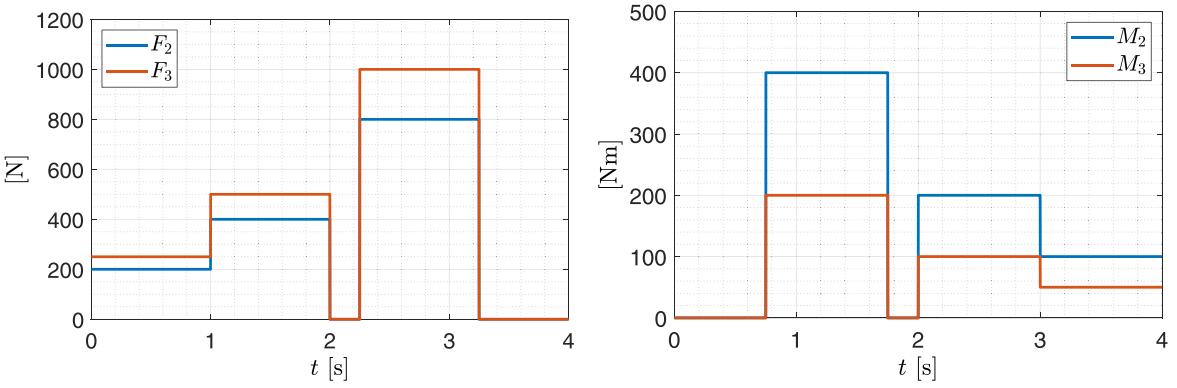

(a) Tip forces. (b) Tip couples.

Fig. 6. 90° circular arch: tip loads time histories. (For interpretation of the references to color in this figure legend, the reader is referred to the web version of this article.)

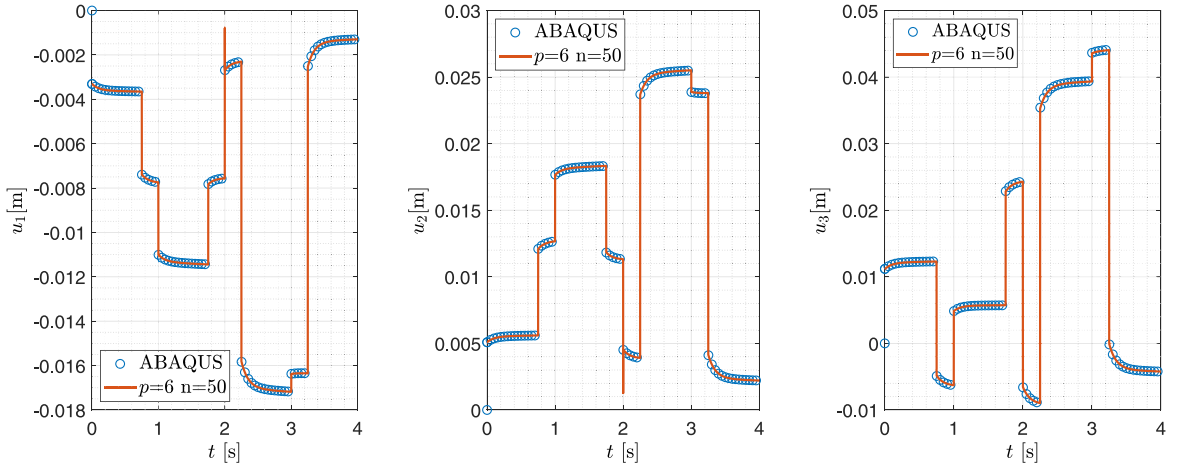

(a) Tip displacement along the x_1-axis. (b) Tip displacement along the x_2-axis. (c) Tip displacement along the x_3-axis.

Fig. 7. 90° circular arch subjected to tip forces and couples.

Table 2
90° circular arch: mechanical properties selected from [109].

	E_α [N/m^2]	τ_α [s]
$\alpha = \infty$	1.419×10^9	–
$\alpha = 1$	2.977×10^8	0.092
$\alpha = 2$	6.363×10^7	0.981
$\alpha = 3$	1.583×10^8	9.527
$\alpha = 4$	1.811×10^8	94.318
$\alpha = 5$	2.388×10^8	920.660
$\alpha = 6$	2.780×10^8	8.998×10^3
$\alpha = 7$	3.277×10^8	8.685×10^4
$\alpha = 8$	3.228×10^8	8.514×10^5
$\alpha = 9$	4.047×10^8	7.740×10^6

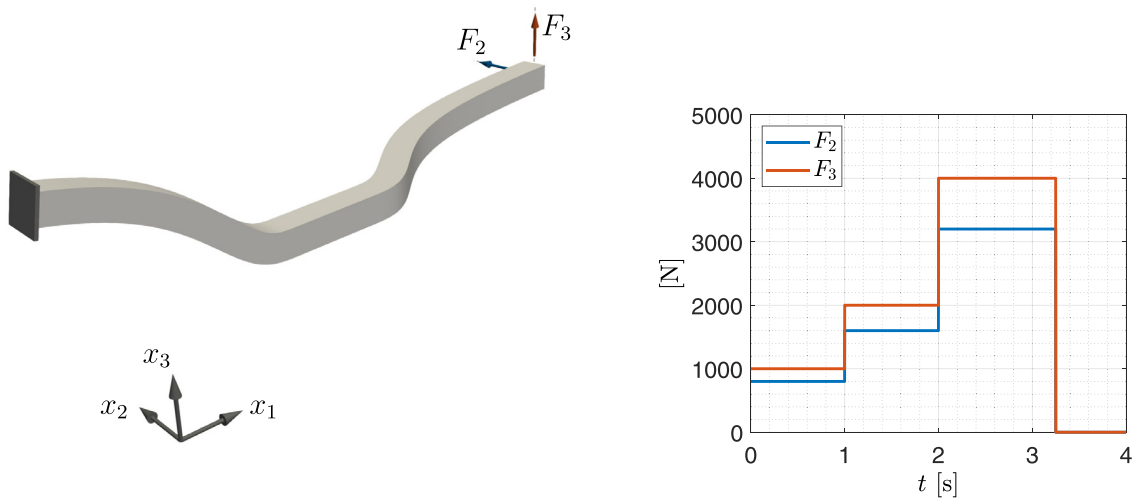

(a) Beam geometry and loads.

(b) Tip forces time history.

Fig. 8. Spivak beam.

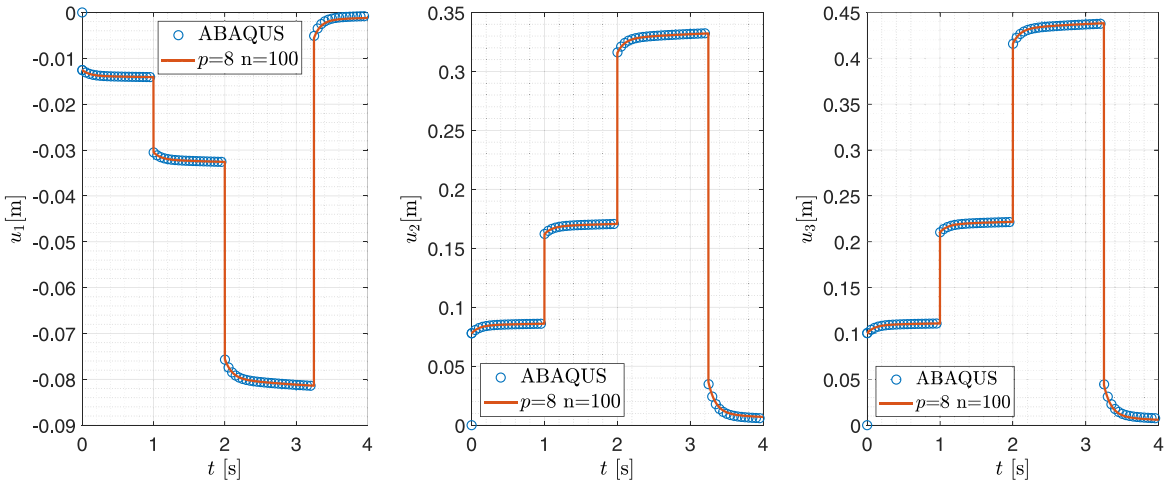

(a) Tip displacement along the x_1-axis.

(b) Tip displacement along the x_2-axis.

(c) Tip displacement along the x_3-axis.

Fig. 9. Spivak beam results comparison.

along the x_2 and the x_3 axes, respectively (see Fig. 8(a)). The time history of the loads is shown in Fig. 8(b). Basis functions with $p = 8$ and $\mathrm{n} = 100$ are used.

Also in this case, for the sake of verification only, the results are compared with Abaqus (B31 elements). Fig. 9 shows the comparison of the tip displacements. The viscous response is very well captured during the time intervals when the loads remain constant. The deformed configuration at $t = 3\,\mathrm{s}$ is shown in Fig. 10.

4.6. Lissajous beam

The Lissajous beam is another geometrically challenging case useful to test the capabilities to model viscoelastic beams with repeated strong curvatures variations. The initial beam axis is defined by the curve $\boldsymbol{c}(s) =$

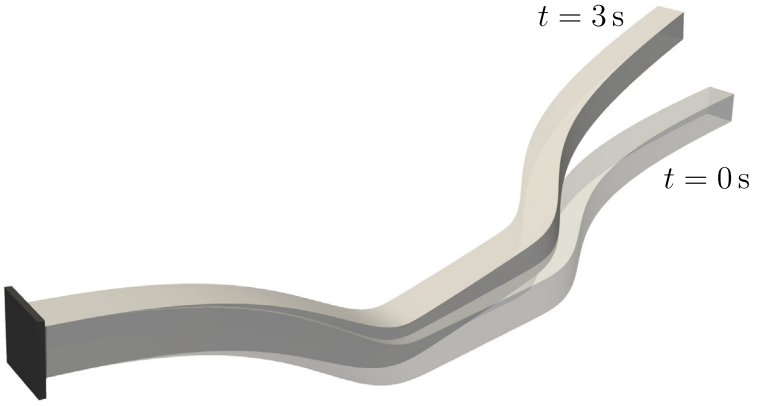

Fig. 10. Spivak beam clamped at one end and subjected to tip forces along x_2-axis and x_3-axis: undeformed configuration (shaded gray) deformed configuration after 3 s (solid gray).

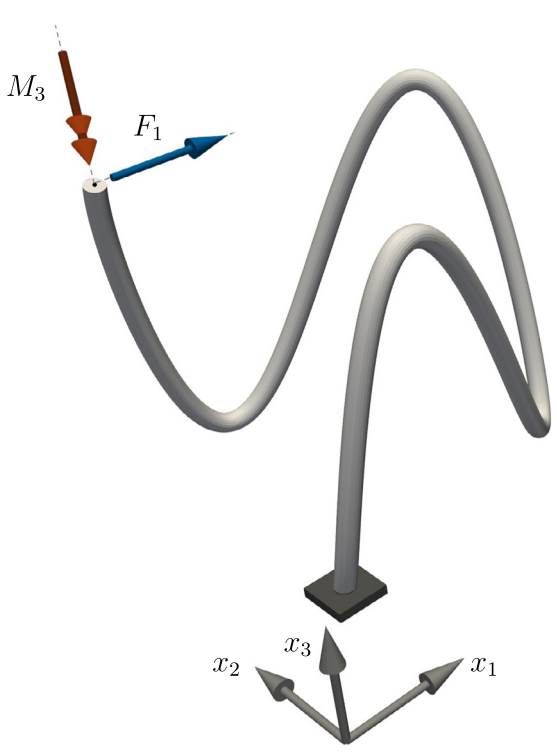

(a) Beam geometry and loads.

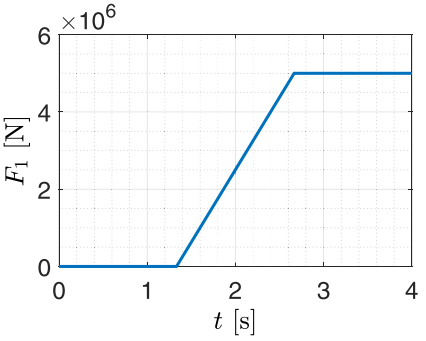

(b) Time history of the tip force, F_1.

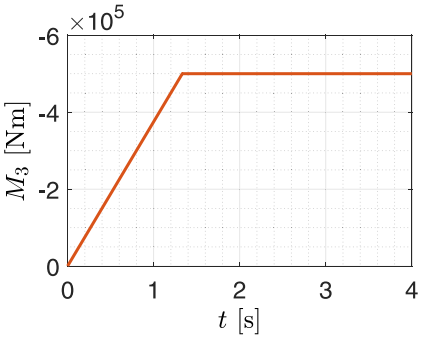

(c) Time history of the tip couple, M_3.

Fig. 11. Lissajous beam.

$[\cos(3s),\ \sin(2s),\ \sin(7s)]^\mathsf{T}$ with $s \in [-\pi/3, \pi/3]$ (see Fig. 11). The beam has a circular cross section of diameter 0.12 m. The viscoelastic material is represented by one Maxwell element with parameters shown in Table 3. A constant Poisson ratio $\nu = 0.4$ is assumed. These material properties are selected from those of the Polylactic acid (PLA) studied in [18].

(a) Deformation at $t = 1.33\,\mathrm{s}$: perspective view.

(b) Deformation at $t = 1.33\,\mathrm{s}$: top view.

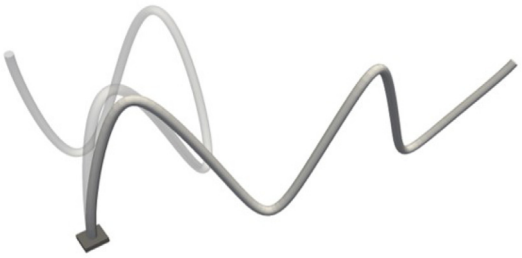

(c) Deformation at $t = 2.67\,\mathrm{s}$: perspective view.

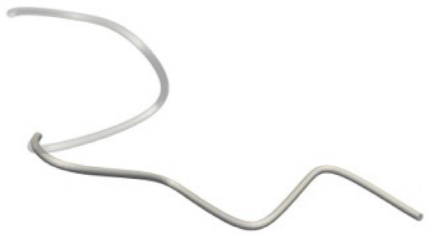

(d) Deformation at $t = 2.67\,\mathrm{s}$: top view.

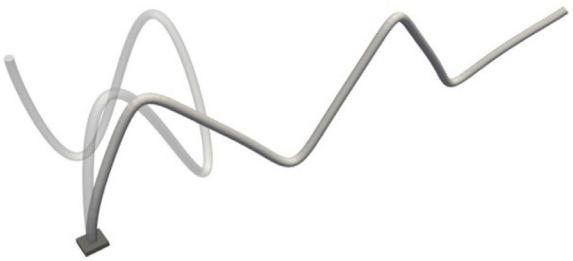

(e) Deformation at $t = 4.00\,\mathrm{s}$: perspective view.

(f) Deformation at $t = 4.00\,\mathrm{s}$: top view.

Fig. 12. Selected snapshots of the complex deformation of the Lissajous beam.

Table 3
Mechanical properties of PLA modeled with a single Maxwell element [18].

	E_α [N/m^2]	τ_α [s]
$\alpha = \infty$	2.80×10^5	–
$\alpha = 1$	3.61×10^7	0.2

The beam is clamped at one end and is loaded at its tip with a negative couple in the x_3 direction and a positive force in the x_1 direction (see Figs. 11(b) and 11(c)).

The test is carried with $\mathrm{n} = 100$ and $p = 8$. The total simulation time is 4 s with a time step $dt = 1 \times 10^{-3}$ s.

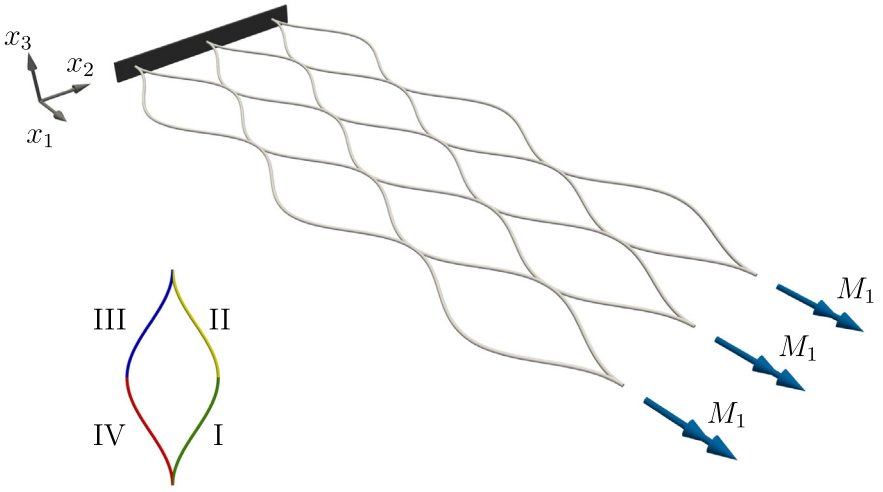

(a) Single cell shape, 3D view and loadings.

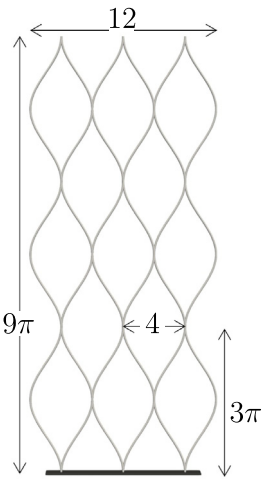

(b) Plane view of the net (units in cm).

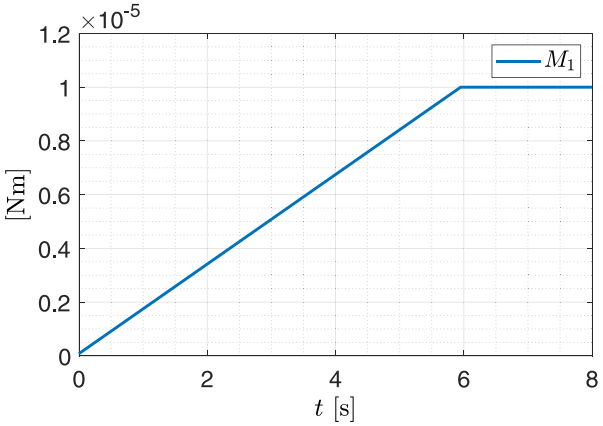

(c) Time-varying loads applied to the free tips of the net.

Fig. 13. Twisting of a planar net made of curved cell elements.

Results are reported in Fig. 12 (left column: perspective views, right column: top views). Figs. 12(a) and 12(b) show the deformed beam configuration at the end of the ramp of the concentrated moment M_3 ($t = 1.33$ s). The beam tends to twist around x_3-axis with respect to its clamped end. Figs. 12(c) and 12(d) show the beam configuration at $t = 2.67$ s, where it is noticeable the joint effect of F_1 and M_3 in straightening the beam. Moreover, it can also be noticed the progressive twisting of the beam around x_3-axis with respect to Figs. 12(a) and 12(b). The final configuration is reported in Figs. 12(e) and 12(f). From $t = 2.67$ s to $t = 4$ s, both F_1 and M_3 are kept constant (see Figs. 11(b) and 11(c)), therefore the additional displacements, observable by comparing Fig. 12(e) with Fig. 12(c), are completely ascribed to viscous effects.

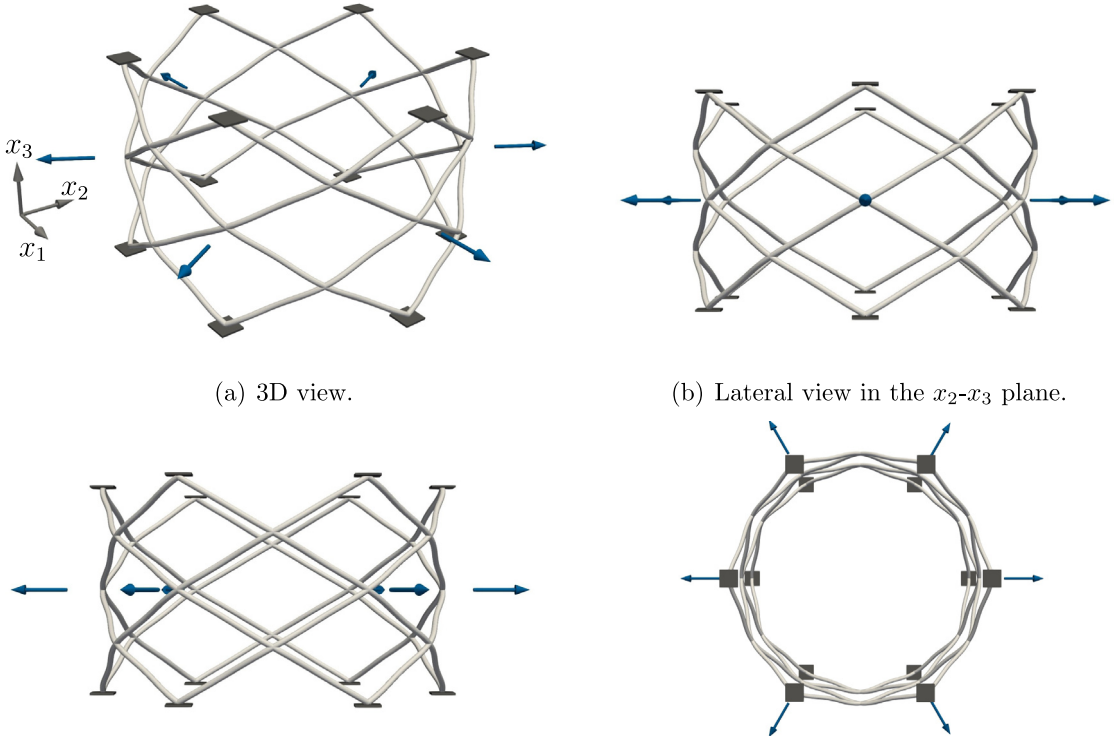

(a) 3D view.

(b) Lateral view in the x_2-x_3 plane.

(c) Lateral view in the x_1-x_3 plane.

(d) Top view in the x_1-x_2 plane.

Fig. 14. Tubular net subjected to concentrated radial forces.

4.7. Planar and tubolar nets with curved cell elements

In the last numerical tests, we address the cases of complex multi-patch structures whose cells are made of curved beam elements. We first consider the case of a planar net and then a cylindrical one (see Figs. 13 and 14). For both cases, the same material of the Lissajous beam is employed with a circular cross section of radius 0.65 mm.

The planar net (Fig. 13) is composed by 36 patches forming a network of 13 closed curved cells (see bottom left of Fig. 13(a)). The centroid line of each patch is a curve described by $\boldsymbol{c}(s) = [1.5s,\ -1^k \sin(s-\pi/2)+2(k-1),\ 0]^\mathsf{T}$, with $s \in [(j-1)\pi, j\pi]$, where $k = 1, 2, \ldots, n_1$ represents the number of subdivisions in the x_1-direction and $j = 1, 2, \ldots, n_2$ the subdivisions in the x_2-direction. Each patch is discretized with basis functions with $p = 8$ and n = 35. The structure is clamped at one end it is loaded with concentrated couples along the x_1-axis along the opposite side. These couples collectively increase linearly from 0 s to 6 s, then they remain constant until 8 s (see Fig. 13(c)).

The second structure is a tubular net (see Fig. 14) consisting in 48 patches connected together to form 12 helical wires. Each patch is described, in a polar coordinate system with $\vartheta \in [0, \pi]$, by the following curve

$$\boldsymbol{c}(s) = [(R + r\cos(\vartheta n_w))\cos(\vartheta),\ (R + r\cos(\vartheta n_w))\sin(\vartheta),\ R\vartheta\tan(\pi/6)]^\mathsf{T}, \tag{37}$$

where $n_w = 4$ denotes the number of patch per wire, while $R = 4 \times 10^{-2}$ m and $r = 6.5 \times 10^{-4}$ m are the outer radius of the tube and the radius of the wires, respectively. Each patch is discretized with basis functions with $p = 8$ and n = 20. The beams system is clamped at both ends and loaded by concentrated radial forces at the nodes of the central section (see Fig. 14). The loads are applied with a linear ramp for 1.15 s, and then kept constant at 1 N until the end of the simulation. The simulation time is 6 s, with $dt = 5 \times 10^{-2}$ s.

Results for the planar net are reported in Figs. 15 and 16 for $t = 2$ s, 4 s, 6 s, and 8 s. Significant viscous deformations are noticeable from $t = 6$ s to $t = 8$ s, that lead to the complete twist of the net with rotations larger than π (see Figs. 16(c) and 16(d)).

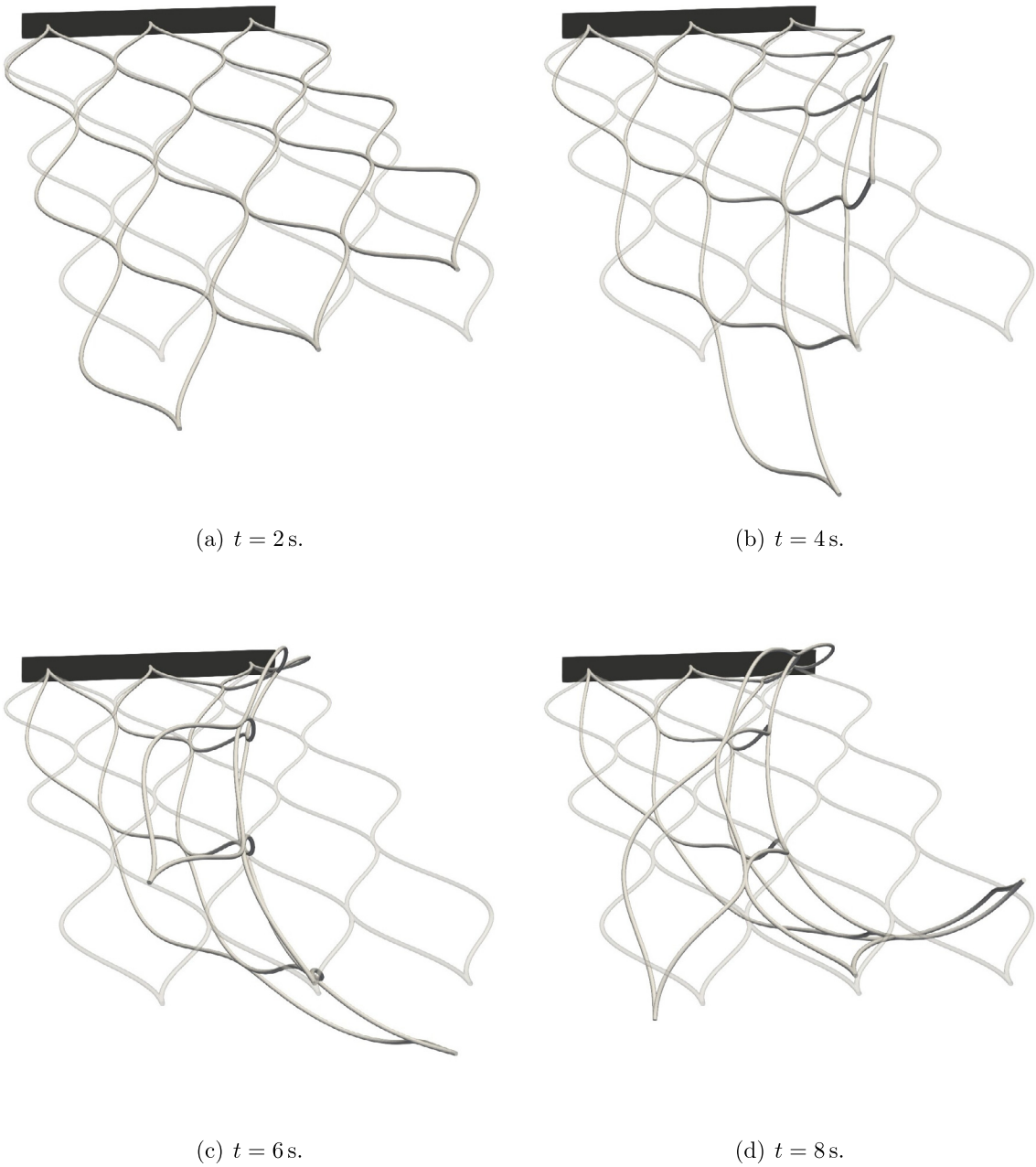

(a) $t = 2\,\mathrm{s}$. (b) $t = 4\,\mathrm{s}$.

(c) $t = 6\,\mathrm{s}$. (d) $t = 8\,\mathrm{s}$.

Fig. 15. Planar net: 3D views of the deformed shape at different time instants.

Fig. 17 shows snapshots of the deformation of the tubular net for $t = 1.15\,\mathrm{s}$, $3.00\,\mathrm{s}$, and $6.00\,\mathrm{s}$. Different lateral views are shown in Figs. 17(a)–17(f), whereas top views are shown in Figs. 17(g)–17(i). The net is locally expanded due to the radial forces and increases its radius of about the 40%.

5. Conclusions

Motivated by the growing demand for fast and accurate simulation tools for materials and objects with architectured inner structures, in this paper we proposed an efficient high-order formulation for geometrically

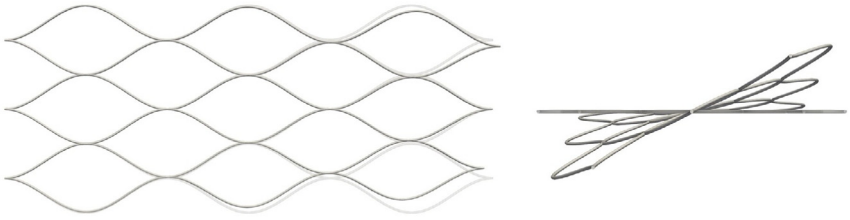

(a) Top and front view, $t = 2\,\mathrm{s}$.

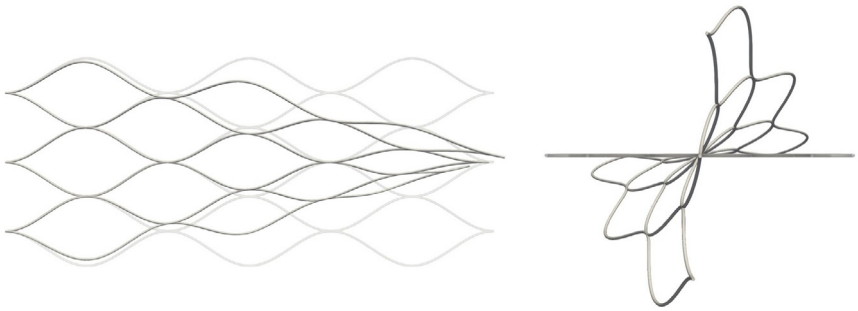

(b) Top and front view, $t = 4\,\mathrm{s}$.

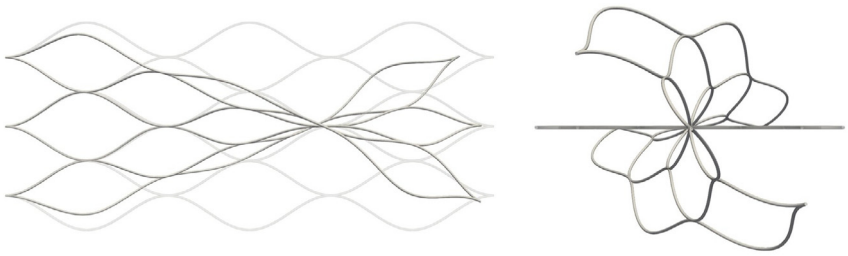

(c) Top and front view, $t = 6\,\mathrm{s}$.

(d) Top and front view, $t = 8\,\mathrm{s}$.

Fig. 16. Planar net: plane views of the deformed shape at different time instants.

exact viscoelastic beams. Linear viscoelasticity is modeled employing the generalized Maxwell model for one-dimensional solids. Very high efficiency is achieved by combining a number of key features. Firstly, the formulation is displacement-based, meaning that the minimal number of equations and unknowns are required. Secondly, for

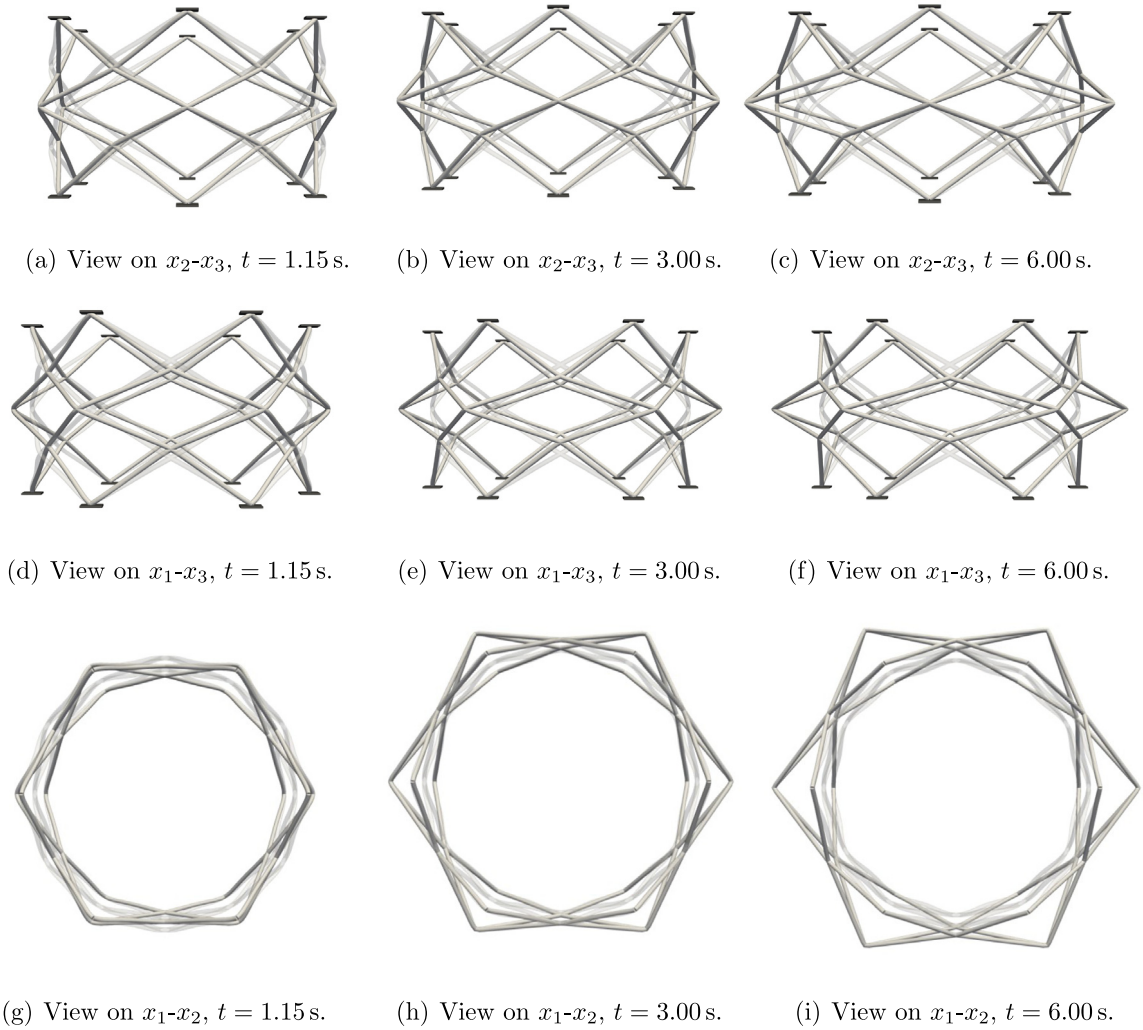

(a) View on x_2-x_3, $t = 1.15\,\mathrm{s}$. (b) View on x_2-x_3, $t = 3.00\,\mathrm{s}$. (c) View on x_2-x_3, $t = 6.00\,\mathrm{s}$.

(d) View on x_1-x_3, $t = 1.15\,\mathrm{s}$. (e) View on x_1-x_3, $t = 3.00\,\mathrm{s}$. (f) View on x_1-x_3, $t = 6.00\,\mathrm{s}$.

(g) View on x_1-x_2, $t = 1.15\,\mathrm{s}$. (h) View on x_1-x_2, $t = 3.00\,\mathrm{s}$. (i) View on x_1-x_2, $t = 6.00\,\mathrm{s}$.

Fig. 17. Tubular net: views of the deformed shape at different time instants.

the spatial discretization we adopted the isogeometric collocation method, which allows to bypass integration over the elements and requires only one point evaluation per unknown. Thirdly, finite rotations are updated using the incremental rotation vector, leading to two main benefits: minimum number of rotation unknowns (namely the three components of the incremental rotation vector) and no singularity problems. Moreover, the formulation has two remarkable advantages: the same SO(3)-consistent linearization of the governing equations and update procedures as for static or dynamic with linear elastic rate-independent materials can be directly used, and the standard second-order accurate trapezoidal rule for time integration turned out to be consistent with the underlying geometric structure of the kinematic problem. High-order space accuracy is obtained exploiting the IGA attributes, especially the tunable smoothness of the basis functions, the ability to accurately reconstruct complex initial geometries, and the k-refinement. Through a number of numerical applications, we demonstrated all the expected features, in particular the high-order accuracy and the robustness in managing arbitrarily complex three-dimensional beam or beams system. In our opinion, the present work opens interesting perspectives towards more efficient simulations of programmable objects, with applications for example to patient-tailored biomedical devices such as cardiovascular stents. Next developments may include, among others, the extension of the formulation to other material models based on internal variables, modeling thermo-responsive materials and, from the kinematic point of view, removing the assumption of rigid beam cross sections.

Declaration of competing interest

The authors declare that they have no known competing financial interests or personal relationships that could have appeared to influence the work reported in this paper.

Data availability

No data was used for the research described in the article.

Acknowledgments

GF and EM were partially supported by the European Union - Next Generation EU, in the context of The National Recovery and Resilience Plan, Investment 1.5 Ecosystems of Innovation, Project Tuscany Health Ecosystem (THE). (CUP: B83C22003920001).

EM was also partially supported by the National Centre for HPC, Big Data and Quantum Computing, Italy funded by the European Union within the Next Generation EU recovery plan. (CUP B83C22002830001).

These supports are gratefully acknowledged.

References

[1] M.F. Ashby, Y.J. Bréchet, Designing hybrid materials, Acta Mater. 51 (19) (2003) 5801–5821.
[2] M. Ashby, Designing architectured materials, Scr. Mater. 68 (1) (2013) 4–7.
[3] S. Xu, Z. Yan, K.-I. Jang, W. Huang, H. Fu, J. Kim, Z. Wei, M. Flavin, J. McCracken, R. Wang, A. Badea, Y. Liu, D. Xiao, G. Zhou, J. Lee, H.U. Chung, H. Cheng, W. Ren, A. Banks, X. Li, U. Paik, R.G. Nuzzo, Y. Huang, Y. Zhang, J.A. Rogers, Assembly of micro/nanomaterials into complex, three-dimensional architectures by compressive buckling, Science 347 (6218) (2015) 154 LP – 159.
[4] S. Li, B. Deng, A. Grinthal, A. Schneider-Yamamura, J. Kang, R.S. Martens, C.T. Zhang, J. Li, S. Yu, K. Bertoldi, J. Aizenberg, Liquid-induced topological transformations of cellular microstructures, Nature 592 (7854) (2021) 386–391.
[5] J.R. Greer, V.S. Deshpande, Three-dimensional architected materials and structures: Design, fabrication, and mechanical behavior, MRS Bull. 44 (10) (2019) 750–757.
[6] Z. Yan, F. Zhang, F. Liu, M. Han, D. Ou, Y. Liu, Q. Lin, X. Guo, H. Fu, Z. Xie, M. Gao, Y. Huang, J.H. Kim, Y. Qiu, K. Nan, J. Kim, P. Gutruf, H. Luo, A. Zhao, K.C. Hwang, Y. Huang, Y. Zhang, J.A. Rogers, Mechanical assembly of complex, 3D mesostructures from releasable multilayers of advanced materials, Sci. Adv. 2 (9) (2016).
[7] Y. Estrin, Y. Beygelzimer, R. Kulagin, P. Gumbsch, P. Fratzl, Y. Zhu, H. Hahn, Architecturing materials at mesoscale: some current trends, Mater. Res. Lett. 9 (10) (2021) 399–421.
[8] X. Cheng, Z. Fan, S. Yao, T. Jin, Z. Lv, Y. Lan, R. Bo, Y. Chen, F. Zhang, Z. Shen, H. Wan, Y. Huang, Y. Zhang, Programming 3D curved mesosurfaces using microlattice designs, Science 379 (6638) (2023) 1225–1232.
[9] Q. Ge, A.H. Sakhaei, H. Lee, C.K. Dunn, N.X. Fang, M.L. Dunn, Multimaterial 4D printing with tailorable shape memory polymers, Sci. Rep. 6 (1) (2016) 31110.
[10] Z. Ding, C. Yuan, X. Peng, T. Wang, H.J. Qi, M.L. Dunn, Direct 4D printing via active composite materials, Sci. Adv. 3 (4) (2017) e1602890.
[11] C.M. Hamel, D.J. Roach, K.N. Long, F. Demoly, M.L. Dunn, H.J. Qi, Machine-learning based design of active composite structures for 4D printing, Smart Mater. Struct. 28 (6) (2019) 065005.
[12] A. Kirillova, L. Ionov, Shape-changing polymers for biomedical applications, J. Mater. Chem. B 7 (10) (2019) 1597–1624.
[13] J.W. Boley, W.M. Van Rees, C. Lissandrello, M.N. Horenstein, R.L. Truby, A. Kotikian, J.A. Lewis, L. Mahadevan, Shape-shifting structured lattices via multimaterial 4D printing, Proc. Natl. Acad. Sci. USA 116 (42) (2019) 20856–20862.
[14] J. Mueller, J.A. Lewis, K. Bertoldi, Architected multimaterial lattices with thermally programmable mechanical response, Adv. Funct. Mater. 32 (1) (2022) 2105128.
[15] A.P. Zakharov, L.M. Pismen, Programmable filaments and textiles, Phys. Rev. Mater. 3 (5) (2019) 055603.
[16] A. Rafsanjani, K. Bertoldi, A.R. Studart, Programming soft robots with flexible mechanical metamaterials, Science Robotics 4 (29) (2019).
[17] B. Florijn, C. Coulais, M. Van Hecke, Programmable mechanical metamaterials: the role of geometry, Soft Matter 12 (42) (2016) 8736–8743.
[18] M. Wan, K. Yu, H. Sun, 4D printed programmable auxetic metamaterials with shape memory effects, Compos. Struct. 279 (2022) 114791.
[19] J.C. Simo, A finite strain beam formulation. The three-dimensional dynamic problem. Part I, Comput. Methods Appl. Mech. Engrg. 49 (1) (1985) 55–70.
[20] J.C. Simo, L. Vu-Quoc, A three-dimensional finite-strain rod model. Part II: Computational aspects, Comput. Methods Appl. Mech. Engrg. 58 (1) (1986) 79–116.
[21] A. Cardona, M. Geradin, A beam finite element non-linear theory with finite rotations, Internat. J. Numer. Methods Engrg. 26 (September 1987) (1988) 2403–2438.

[22] E.N. Dvorkin, E. Onte, J. Oliver, On a non-linear formulation for curved timoshenko beam elements considering large displacement/rotation increments, Internat. J. Numer. Methods Engrg. 26 (7) (1988) 1597–1613.
[23] M. Crisfield, A consistent co-rotational formulation for non-linear, three-dimensional, beam-elements, Comput. Methods Appl. Mech. Engrg. 81 (2) (1990) 131–150.
[24] A. Ibrahimbegovic, On finite element implementation of geometrically nonlinear Reissner's beam theory: three-dimensional curved beam elements, Comput. Methods Appl. Mech. Engrg. 122 (1–2) (1995) 11–26.
[25] A. Ibrahimbegović, F. Frey, I. Kožar, Computational aspects of vector-like parametrization of three-dimensional finite rotations, Internat. J. Numer. Methods Engrg. 38 (21) (1995) 3653–3673.
[26] A. Ibrahimbegovic, On the choice of finite rotation parameters, Comput. Methods Appl. Mech. Eng. 149 (3) (1997) 49–71.
[27] G. Jelenić, M. Crisfield, Geometrically exact 3D beam theory: implementation of a strain-invariant finite element for statics and dynamics, Comput. Methods Appl. Mech. Engrg. 171 (1–2) (1999) 141–171.
[28] I. Romero, F. Armero, An objective finite element approximation of the kinematics of geometrically exact rods and its use in the formulation of an energy-momentum conserving scheme in dynamics, Internat. J. Numer. Methods Engrg. 54 (12) (2002) 1683–1716.
[29] I. Romero, The interpolation of rotations and its application to finite element models of geometrically exact rods, Comput. Mech. 34 (2) (2004) 121–133.
[30] M. Ritto-Correa, D. Camotim, On the differentiation of the Rodrigues formula and its significance for the vector-like parameterization of Reissner-Simo beam theory, Internat. J. Numer. Methods Engrg. 55 (9) (2002) 1005–1032.
[31] P. Betsch, P. Steinmann, Frame-indifferent beam finite elements based upon the geometrically exact beam theory, Internat. J. Numer. Methods Engrg. 54 (12) (2002) 1775–1788.
[32] D. Magisano, L. Leonetti, A. Madeo, G. Garcea, A large rotation finite element analysis of 3D beams by incremental rotation vector and exact strain measure with all the desirable features, Comput. Methods Appl. Mech. Engrg. 361 (2020) 112811.
[33] D. Magisano, L. Leonetti, G. Garcea, Isogeometric analysis of 3D beams for arbitrarily large rotations: Locking-free and path-independent solution without displacement DOFs inside the patch, Comput. Methods Appl. Mech. Engrg. 373 (2021) 113437.
[34] D. Vo, P. Nanakorn, T.Q. Bui, Geometrically nonlinear multi-patch isogeometric analysis of spatial Euler–Bernoulli beam structures, Comput. Methods Appl. Mech. Engrg. 380 (2021) 113808.
[35] L. Greco, M. Cuomo, D. Castello, A. Scrofani, An updated Lagrangian Bézier finite element formulation for the analysis of slender beams, Math. Mech. Solids 27 (10) (2022) 2110–2138.
[36] A. Borković, B. Marussig, G. Radenković, Geometrically exact static isogeometric analysis of an arbitrarily curved spatial Bernoulli–Euler beam, Comput. Methods Appl. Mech. Engrg. 390 (2022) 114447.
[37] A. Borković, M.H. Gfrerer, B. Marussig, Geometrically exact isogeometric Bernoulli–Euler beam based on the Frenet–Serret frame, Comput. Methods Appl. Mech. Engrg. 405 (2023) 115848.
[38] M.S. Park, B.C. Lee, Geometrical non-linear and elastoplastic three-dimensional shear flexible beam element of von-Mises-type hardening materials, Internat. J. Numer. Methods Engrg. 39 (3) (1996) 383–408.
[39] F. Gruttmann, R. Sauer, W. Wagner, Theory and numerics of three-dimensional beams with elastoplastic material behaviour §, Internat. J. Numer. Methods Engrg. 48 (2000) 1675–1702.
[40] J.M. Battini, C. Pacoste, Plastic instability of beam structures using co-rotational elements, Comput. Methods Appl. Mech. Engrg. 191 (51–52) (2002) 5811–5831.
[41] S. Smriti, A. Kumar, P. Steinmann, A finite element formulation for a direct approach to elastoplasticity in special Cosserat rods, Internat. J. Numer. Methods Engrg. 122 (5) (2021) 1262–1282.
[42] L. Herrnböck, A. Kumar, P. Steinmann, Geometrically exact elastoplastic rods: determination of yield surface in terms of stress resultants, Comput. Mech. 67 (3) (2021) 723–742.
[43] L. Herrnböck, A. Kumar, P. Steinmann, Two-scale off-and online approaches to geometrically exact elastoplastic rods, Comput. Mech. 71 (1) (2023) 1–24.
[44] L.G. Maqueda, A.A. Shabana, Poisson modes and general nonlinear constitutive models in the large displacement analysis of beams, Multibody Syst. Dyn. 18 (3) (2007) 375–396.
[45] P. Mata, S. Oller, A.H. Barbat, Static analysis of beam structures under nonlinear geometric and constitutive behavior, Comput. Methods Appl. Mech. Engrg. 196 (45–48) (2007) 4458–4478.
[46] P. Mata, S. Oller, A.H. Barbat, Dynamic analysis of beam structures considering geometric and constitutive nonlinearity, Comput. Methods Appl. Mech. Engrg. 197 (6–8) (2008) 857–878.
[47] J. Wackerfuß, F. Gruttmann, A mixed hybrid finite beam element with an interface to arbitrary three-dimensional material models, Comput. Methods Appl. Mech. Engrg. 198 (27–29) (2009) 2053–2066.
[48] J. Wackerfuß, F. Gruttmann, A nonlinear Hu–Washizu variational formulation and related finite-element implementation for spatial beams with arbitrary moderate thick cross-sections, Comput. Methods Appl. Mech. Engrg. 200 (17–20) (2011) 1671–1690.
[49] S. Klinkel, S. Govindjee, Using finite strain 3D-material models in beam and shell elements, Eng. Comput. 19 (3) (2002) 254–271.
[50] M.J. Choi, R.A. Sauer, S. Klinkel, An isogeometric finite element formulation for geometrically exact timoshenko beams with extensible directors, Comput. Methods Appl. Mech. Engrg. 385 (2021) 113993.
[51] M.J. Choi, S. Klinkel, R.A. Sauer, An isogeometric finite element formulation for frictionless contact of Cosserat rods with unconstrained directors, Comput. Mech. 70 (6) (2022) 1107–1144.
[52] H. Lang, J. Linn, M. Arnold, Multi-body dynamics simulation of geometrically exact Cosserat rods, Multibody Syst. Dyn. 25 (3) (2011) 285–312.
[53] H. Lang, M. Arnold, Numerical aspects in the dynamic simulation of geometrically exact rods, Appl. Numer. Math. 62 (10) (2012) 1411–1427.

[54] J. Linn, H. Lang, A. Tuganov, Geometrically exact Cosserat rods with Kelvin–Voigt type viscous damping, Mech. Sci. 4 (1) (2013) 79–96.
[55] G.G. Giusteri, E. Miglio, N. Parolini, M. Penati, R. Zambetti, Simulation of viscoelastic Cosserat rods based on the geometrically exact dynamics of special Euclidean strands, Internat. J. Numer. Methods Engrg. 123 (2) (2022) 396–410.
[56] Y. Zhang, Q. Tian, L. Chen, J.J. Yang, Simulation of a viscoelastic flexible multibody system using absolute nodal coordinate and fractional derivative methods, Multibody Syst. Dyn. 21 (3) (2008) 281–303.
[57] A.N.A. Mohamed, A.A. Shabana, A nonlinear visco-elastic constitutive model for large rotation finite element formulations, Multibody Syst. Dyn. 26 (1) (2011) 57–79.
[58] O.A. Bauchau, N. Nemani, Modeling viscoelastic behavior in flexible multibody systems, Multibody Syst. Dyn. 51 (2) (2021) 159–194.
[59] O. Weeger, S.-K. Yeung, M.L. Dunn, Fully isogeometric modeling and analysis of nonlinear 3D beams with spatially varying geometric and material parameters, Comput. Methods Appl. Mech. Engrg. 342 (2018) 95–115.
[60] Z. Ding, O. Weeger, H.J. Qi, M.L. Dunn, 4D rods: 3D structures via programmable 1D composite rods, Mater. Des. 137 (2018) 256–265.
[61] A. Zakharov, L.M. Pismen, L. Ionov, Shape-morphing architectures actuated by Janus fibers, Soft Matter 16 (8) (2020) 2086–2092.
[62] O. Weeger, B. Narayanan, M.L. Dunn, Isogeometric shape optimization of nonlinear, curved 3D beams and beam structures, Comput. Methods Appl. Mech. Engrg. 345 (2019) 26–51.
[63] B. Audoly, N. Clauvelin, P.T. Brun, M. Bergou, E. Grinspun, M. Wardetzky, A discrete geometric approach for simulating the dynamics of thin viscous threads, J. Comput. Phys. 253 (2013) 18–49.
[64] C. Lestringant, B. Audoly, D.M. Kochmann, A discrete, geometrically exact method for simulating nonlinear, elastic and inelastic beams, Comput. Methods Appl. Mech. Engrg. 361 (2020) 112741.
[65] C. Lestringant, D.M. Kochmann, Modeling of flexible beam networks and morphing structures by geometrically exact discrete beams, J. Appl. Mech. Trans. ASME 87 (8) (2020).
[66] R.N. Glaesener, J.-H. Bastek, F. Gonon, V. Kannan, B. Telgen, B. Spöttling, S. Steiner, D.M. Kochmann, Viscoelastic truss metamaterials as time-dependent generalized continua, J. Mech. Phys. Solids 156 (2021) 104569.
[67] O. Weeger, D. Schillinger, R. Müller, Mixed isogeometric collocation for geometrically exact 3D beams with elasto-visco-plastic material behavior and softening effects, Comput. Methods Appl. Mech. Engrg. 399 (2022) 115456.
[68] H. Le Clézio, C. Lestringant, D.M. Kochmann, A numerical two-scale approach for nonlinear hyperelastic beams and beam networks, Int. J. Solids Struct. (2023) 112307.
[69] V.X. Nguyen, K.T. Nguyen, S. Thai, Large deflection analysis of functionally graded beams based on geometrically exact three-dimensional beam theory and isogeometric analysis, Int. J. Non-Linear Mech. 146 (2022) 104152.
[70] K. Bertoldi, V. Vitelli, J. Christensen, M. van Hecke, Flexible mechanical metamaterials, Nat. Rev. Mater. 2 (11) (2017) 17066.
[71] D.M.J. Dykstra, J. Busink, B. Ennis, C. Coulais, Viscoelastic snapping metamaterials, J. Appl. Mech. 86 (11) (2019).
[72] S. Janbaz, K. Narooei, T. van Manen, A.A. Zadpoor, Strain rate-dependent mechanical metamaterials, Sci. Adv. 6 (25) (2020) eaba0616.
[73] M. Gavazzoni, S. Foletti, D. Pasini, Cyclic response of 3D printed metamaterials with soft cellular architecture: The interplay between as-built defects, material and geometric non-linearity, J. Mech. Phys. Solids 158 (2022) 104688.
[74] F. Auricchio, L. Beirão Da Veiga, T.J.R. Hughes, A. Reali, G. Sangalli, Isogeometric collocation methods, Math. Models Methods Appl. Sci. 20 (11) (2010) 2075–2107.
[75] F. Auricchio, L. Beirão da Veiga, T.J.R. Hughes, A. Reali, G. Sangalli, Isogeometric collocation for elastostatics and explicit dynamics, Comput. Methods Appl. Mech. Engrg. 249–252 (2012) 2–14.
[76] F. Fahrendorf, S. Shivanand, B.V. Rosic, M.S. Sarfaraz, T. Wu, L. De Lorenzis, H.G. Matthies, Collocation methods and beyond in non-linear mechanics, in: J. Schröder, P. Wriggers (Eds.), Non-Standard Discretisation Methods in Solid Mechanics, Springer International Publishing, Cham, 2022, pp. 449–504.
[77] T. Hughes, J. Cottrell, Y. Bazilevs, Isogeometric analysis: CAD, finite elements, NURBS, exact geometry and mesh refinement, Comput. Methods Appl. Mech. Engrg. 194 (39–41) (2005) 4135–4195.
[78] J.A. Cottrell, T.J.R. Hughes, Y. Bazilevs, Isogeometric Analysis: Toward Integration of CAD and FEA, Wiley, 2009.
[79] D. Schillinger, J. Evans, A. Reali, M. Scott, T.J.R. Hughes, Isogeometric collocation: Cost comparison with Galerkin methods and extension to adaptive hierarchical NURBS discretizations, Comput. Methods Appl. Mech. Engrg. 267 (2013) 170–232.
[80] H. Gomez, A. Reali, G. Sangalli, Accurate, efficient, and (iso)geometrically flexible collocation methods for phase-field models, J. Comput. Phys. 262 (2014) 153–171.
[81] L. De Lorenzis, J. Evans, T. Hughes, A. Reali, Isogeometric collocation: Neumann boundary conditions and contact, Comput. Methods Appl. Mech. Engrg. 284 (2015) 21–54.
[82] R. Kruse, N. Nguyen-Thanh, L. De Lorenzis, T. Hughes, Isogeometric collocation for large deformation elasticity and frictional contact problems, Comput. Methods Appl. Mech. Engrg. 296 (2015) 73–112.
[83] H. Gomez, L. De Lorenzis, The variational collocation method, Comput. Methods Appl. Mech. Engrg. 309 (2016) 152–181.
[84] L. Beirão da Veiga, C. Lovadina, a. Reali, Avoiding shear locking for the Timoshenko beam problem via isogeometric collocation methods, Comput. Methods Appl. Mech. Engrg. 241–244 (2012) 38–51.
[85] F. Auricchio, L. Beirão da Veiga, J. Kiendl, C. Lovadina, A. Reali, Locking-free isogeometric collocation methods for spatial Timoshenko rods, Comput. Methods Appl. Mech. Engrg. 263 (2013) 113–126.
[86] J. Kiendl, F. Auricchio, T. Hughes, A. Reali, Single-variable formulations and isogeometric discretizations for shear deformable beams, Comput. Methods Appl. Mech. Engrg. 284 (2015) 988–1004.
[87] J. Kiendl, F. Auricchio, A. Reali, A displacement-free formulation for the Timoshenko beam problem and a corresponding isogeometric collocation approach, Meccanica (2017) 1–11.

[88] G. Balduzzi, S. Morganti, F. Auricchio, Non-prismatic Timoshenko-like beam model: Numerical solution via isogeometric collocation, Comput. Math. Appl. 74 (7) (2017) 1531–1541.
[89] A. Reali, H. Gomez, An isogeometric collocation approach for Bernoulli-Euler beams and Kirchhoff plates, Comput. Methods Appl. Mech. Engrg. 284 (2015) 623–636.
[90] J. Kiendl, F. Auricchio, L. Beirão da Veiga, C. Lovadina, A. Reali, Isogeometric collocation methods for the Reissner-Mindlin plate problem, Comput. Methods Appl. Mech. Engrg. 284 (2015) 489–507.
[91] J. Kiendl, E. Marino, L. De Lorenzis, Isogeometric collocation for the Reissner-Mindlin shell problem, Comput. Methods Appl. Mech. Engrg. 325 (2017) 645–665.
[92] F. Maurin, F. Greco, L. Coox, D. Vandepitte, W. Desmet, Isogeometric collocation for Kirchhoff-Love plates and shells, Comput. Methods Appl. Mech. Engrg. 329 (2018) 396–420.
[93] F. Maurin, F. Greco, S. Dedoncker, W. Desmet, Isogeometric analysis for nonlinear planar Kirchhoff rods: Weighted residual formulation and collocation of the strong form, Comput. Methods Appl. Mech. Engrg. (2018).
[94] J.A. Evans, R.R. Hiemstra, T.J.R. Hughes, A. Reali, Explicit higher-order accurate isogeometric collocation methods for structural dynamics, Comput. Methods Appl. Mech. Engrg. 338 (2018) 208–240.
[95] F. Fahrendorf, S. Morganti, A. Reali, T.J. Hughes, L.D. Lorenzis, Mixed stress-displacement isogeometric collocation for nearly incompressible elasticity and elastoplasticity, Comput. Methods Appl. Mech. Engrg. 369 (2020) 113112.
[96] E. Marino, S.F. Hosseini, A. Hashemian, A. Reali, Effects of parameterization and knot placement techniques on primal and mixed isogeometric collocation formulations of spatial shear-deformable beams with varying curvature and torsion, Comput. Math. Appl. 80 (11) (2020) 2563–2585.
[97] M. Torre, S. Morganti, A. Nitti, M.D. de Tullio, F.S. Pasqualini, A. Reali, Isogeometric mixed collocation of nearly-incompressible electromechanics in finite deformations for cardiac muscle simulations, Comput. Methods Appl. Mech. Engrg. 411 (2023) 116055.
[98] E. Marino, Isogeometric collocation for three-dimensional geometrically exact shear-deformable beams, Comput. Methods Appl. Mech. Engrg. 307 (2016) 383–410.
[99] O. Weeger, S.-K. Yeung, M.L. Dunn, Isogeometric collocation methods for Cosserat rods and rod structures, Comput. Methods Appl. Mech. Engrg. 316 (2017) 100–122.
[100] E. Marino, Locking-free isogeometric collocation formulation for three-dimensional geometrically exact shear-deformable beams with arbitrary initial curvature, Comput. Methods Appl. Mech. Engrg. 324 (2017) 546–572.
[101] E. Marino, J. Kiendl, L. De Lorenzis, Explicit isogeometric collocation for the dynamics of three-dimensional beams undergoing finite motions, Comput. Methods Appl. Mech. Engrg. 343 (2019) 530–549.
[102] E. Marino, J. Kiendl, L. De Lorenzis, Isogeometric collocation for implicit dynamics of three-dimensional beams undergoing finite motions, Comput. Methods Appl. Mech. Engrg. 356 (2019) 548–570.
[103] D. Ignesti, G. Ferri, F. Auricchio, A. Reali, E. Marino, An improved isogeometric collocation formulation for spatial multi-patch shear-deformable beams with arbitrary initial curvature, Comput. Methods Appl. Mech. Engrg. 403 (2023) 115722.
[104] R.M. Christensen, Theory of Viscoelasticity: Second Edition, in: Dover Civil and Mechanical Engineering, Dover Publications, 2013.
[105] M.A. Crisfield, G. Jelenić;, Objectivity of strain measures in the geometrically exact three-dimensional beam theory and its finite-element implementation, Proc. R. Soc. A 455 (1983) (1999) 1125–1147.
[106] R.K. Kapania, J. Li, On a geometrically exact curved/twisted beam theory under rigid cross-section assumption, Comput. Mech. 30 (5–6) (2003) 428–443.
[107] Y. Choquet-Bruhat, C. Dewitt-Morette, Analysis, Manifolds and Physics Part I: Basics, Elsevier B.V., 1996.
[108] Abaqus, Abaqus 6.11 Theory Manual.
[109] G.S. Payette, J.N. Reddy, A nonlinear finite element framework for viscoelastic beams based on the high-order reddy beam theory, Trans. ASME, J. Mech. Des. 135 (1) (2013).